ANNUAL REVIEWS

Annual Review of Earth and Planetary Sciences

Seismic and Electrical Signatures of the Lithosphere–Asthenosphere System of the Normal Oceanic Mantle

Hitoshi Kawakatsu and Hisashi Utada

Earthquake Research Institute, The University of Tokyo, Tokyo 113-0032, Japan;
email: hitosi@eri.u-tokyo.ac.jp

Annu. Rev. Earth Planet. Sci. 2017. 45:139–67

The *Annual Review of Earth and Planetary Sciences* is online at earth.annualreviews.org

https://doi.org/10.1146/annurev-earth-063016-020319

Keywords

lithosphere, asthenosphere, Lid, low-velocity zone, G-discontinuity, plate tectonics, anisotropy, electrical conductivity

Abstract

Although plate tectonics started as a theory of the ocean basins nearly 50 years ago, the mechanical details of how it works are still poorly known. Our understanding of these details has been hampered partly by our inability to characterize the physical nature of the lithosphere–asthenosphere system (LAS) beneath the ocean. We review the existing observational constraints on the seismic and electrical properties of the LAS, particularly for normal oceanic regions away from mid-oceanic ridges, hot spots, and subduction zones, where plate tectonics is expected to present its simplest form. Whereas a growing volume of seismic data on land has provided remarkable advances in large-scale pictures, seafloor observations have been shedding new light on essential details. By combing through these observational constraints, researchers are unveiling the nature of the enigmatic LAS. Future directions for large-scale seafloor observations are also discussed.

1. INTRODUCTION: LITHOSPHERE–ASTHENOSPHERE SYSTEM IN THE OCEAN

LAS: lithosphere–asthenosphere system

LAB: lithosphere–asthenosphere boundary

LVZ: low-velocity zone

LCL: low-conductivity layer

HCL: high-conductivity layer

EM: electromagnetic

Plate tectonics, a phenomenological framework describing the motions of the solid Earth, is based on the concept that a small number of rigid shells that cover Earth's surface move horizontally relative to each other, making earthquakes and volcanoes at and around their boundaries. To facilitate such motions, the rigid surface part of Earth comprising its plates, the lithosphere, is believed to sit on top of a weak layer, the asthenosphere, and thus elucidation of the lithosphere and asthenosphere as a whole is essential for understanding how our planet works. Considering that the lithosphere is created from the mantle, i.e., asthenosphere, at ridges beneath the ocean and that it thermally thickens (ages) as it moves away from these ridges, the lithosphere and the asthenosphere need to be understood together as an evolving system. Thus, elucidation of the lithosphere–asthenosphere system (LAS) has been the focus of recent observational geophysics.

Although advances in seismic tomography and numerical simulations of mantle convection over the past 30 years or so have greatly improved our understanding of how plate tectonics might be related to processes occurring in the deep interior of Earth, the physical conditions that distinguish the lithosphere and asthenosphere are under debate. The complicated history of the evolution of the continents makes it difficult to resolve this fundamental question using observations under the continents. In contrast, plate tectonics is expected to show its simplest representation of the LAS under the oceans. Thus, better observational constraints are expected from the oceanic crust and mantle, although great challenges exist from the observational point of view. This article reviews recent progress in this direction. We concentrate on properties of the normal oceanic mantle, staying away from popular science targets, such as mid-oceanic ridges, hot spots (seamounts), and subduction zones (and also the crustal structure).

1.1. Mechanical Layering

Figure 1 illustrates two schematic views of the LAS in the ocean that may be seen in textbooks. The terms "lithosphere" and "asthenosphere" refer to tectonic/dynamic layering in the suboceanic mantle on the basis of mechanical strength. The lithosphere is Earth's rigid outermost shell and consists of the crust and the uppermost part of the upper mantle; it is considered equivalent with the term "plate" in the context of plate tectonics. The asthenosphere, named after the Greek word meaning "weak," is a soft layer of the mantle, just below the lithosphere, that facilitates horizontal movements of plates. The word existed even in the early 1900s, before the birth of plate tectonics, to explain the long-term ground deformation associated with the removal of Pleistocene glaciers. Recent literature discusses what defines the lithosphere–asthenosphere boundary (LAB), and some researchers argue that the boundary could be transitional rather than sharp.

1.2. Seismic and Electrical Layering

Seismic velocity layering typically indicates a thin (~6-km) oceanic crust (White et al. 1992) underlaid by a nearly constant high-velocity layer (Lid) and a low-velocity zone (LVZ) (Gutenberg 1959). The sharp velocity decrease from Lid to LVZ is called the G-discontinuity after Beno Gutenberg (Revenaugh & Jordan 1991). Some recent seismological literature refers to such discontinuous structures as the LAB, which may be somewhat misleading, as from seismology alone there is no simple way to tell whether a structure is the true LAB. Similarly, electrical conductivity layering shows a low-conductivity layer (LCL) underlaid by a high-conductivity layer (HCL). As the transition thickness from LCL to HCL is difficult to constrain from electromagnetic (EM) data, no boundary structure is usually reported for the electrical conductivity. The Lid/LCL

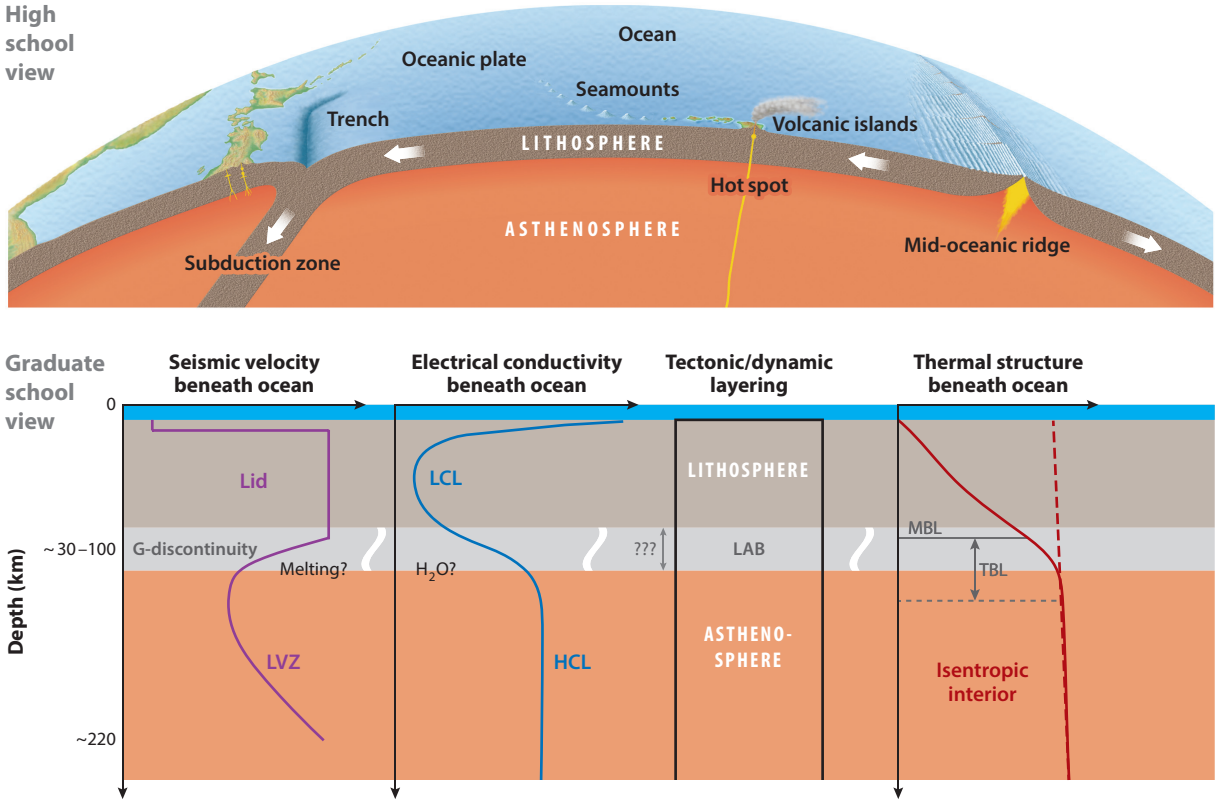

Figure 1

(*Top*) High school and (*bottom*) graduate school textbook views of the oceanic lithosphere–asthenosphere system. Abbreviations: HCL, high-conductivity layer; LAB, lithosphere–asthenosphere boundary; LCL, low-conductivity layer; LVZ, low-velocity zone; MBL, mechanical boundary layer; TBL, thermal boundary layer. Top panel adapted from *Basic Earth Science*, revised edition, Keirinkan.

and LVZ/HCL are often associated with the lithosphere and asthenosphere, respectively, and G-discontinuity with the LAB. It is not obvious, however, that such a simple association is meaningful. Characterizing seismic and electrical structures from observations, as well as discussing their origins in terms of dynamic layering, has been a topic of great interest in recent studies.

Theoretical estimates of how mantle rocks behave with depth indicate that the competing effects of temperature and pressure cause a seismic velocity minimum in the depth range ~100–150 km beneath the ocean, the depth range of the LVZ (Stixrude & Lithgow-Bertelloni 2005). The question is whether this LVZ is weak or viscous enough to be consistent with the geodynamical properties required for the asthenosphere (e.g., Richards et al. 2001). Another question is how gradual changes of temperature and pressure could cause the large seismic velocity reduction reported at the G-discontinuity at a depth of ~30–100 km beneath the ocean.

1.3. Thermal Structure

Ocean-floor subsidence and heat-flow decrease as plates cool with age are well modeled by the plate model (e.g., Parsons & Sclater 1977), and the thermal structure beneath the ocean may be approximated by a shallow linear gradient zone and a deeper isentropic convecting interior. The

transition between these layers is called the thermal boundary layer (TBL) by Parsons & McKenzie (1978), where small-scale convection might be taking place to transport heat from below. Above the TBL, there is a mechanical boundary layer (MBL) that may be equated with the lithosphere. Incorporating gravity data, Crosby et al. (2006) estimated the cross point of the two linear thermal gradients at a depth of 90 km for old Pacific Ocean, which might give a deepest possible depth of the lithosphere (i.e., lower boundary of the MBL).

TBL: thermal boundary layer

MBL: mechanical boundary layer

1.4. Melts and Volatiles

The presence of partial melt has a strong influence on the physical properties of mantle rocks. Seismic velocity of mantle rocks decreases and electrical conductivity increases where melts exist. Therefore, the presence of partial melt was suggested to account for the origin of the LVZ and the HCL in the upper mantle (Anderson & Sammis 1970, Shankland & Waff 1977). However, the connection between physical properties of the melt phase and of the bulk partially molten rock is not simple. The geometry of melt phases (or aqueous fluids) has significant effects on the velocity change that might be inferred from seismic observations (Takei 2002). The connectivity of the melt phase has a significant influence on electrical properties (Toramaru & Fujii 1986). However, once a well-connected melt network is formed in a partially molten system, the bulk electrical conductivity does not depend much on the texture of the network but is simply proportional to the fraction and connectivity of melt (Utada & Baba 2014).

A certain quantity of volatiles is expected in the mantle, and H_2O and CO_2 in particular are considered to play important roles in controlling the physical properties of that region. Geochemical studies suggest the water content to be about 100 ppm H_2O and the mass ratio H/C to be about 0.75 in the typical suboceanic mantle (Hirschmann & Dasgupta 2009). Deformation experiments showed that even a small amount (only a few ppm by weight) of water will enhance the creep rate of olivine by orders of magnitude (Mei & Kohlstedt 2000a,b). However, a recent study cast doubt on this result, reporting a rather weak effect of water on upper-mantle rheology (Fei et al. 2013). Water (hydrogen) dissolved in mantle minerals is also considered to reduce seismic velocity and to enhance electrical conductivity, but the significance of these effects is not well resolved. The water effect on electrical conductivity is especially controversial, and significant inconsistency among experimental results obtained by different groups has prevented conclusive, quantitative interpretation of the geophysical data (Gardes et al. 2014).

In addition, volatiles (H_2O or CO_2) in the upper mantle, even in small amounts, significantly reduce the solidus temperature, which is effective in producing partial melting in the upper mantle. In the presence of volatiles at likely concentration, most of the oceanic LVZ and HCL is either close to or above the solidus temperature of hydrated or carbonated peridotite. Stability calculations of partial melt (Hirschmann 2010) indicate large spatial variations of partial melts, with different H_2O and CO_2 concentrations depending on different degrees of melting. At a low degree of melting, melt contains high concentrations of CO_2 and is called carbonatite melt. Recent experimental studies report that carbonatite melt has extremely high electrical conductivity (e.g., Gaillard et al. 2008, Yoshino & Katsura 2013).

2. GLOBAL AND LAND-BASED STUDIES

Extensive seismological investigation of the oceanic LAS has been conducted by employing surface-wave dispersion measurements from land-based seismic stations. Surface waves propagate effectively in the oceanic region, and at long periods (say, longer than ~30 s) they dominate the wavefield, making for easy observation. The surface-wave dispersion curve, that is, the period

dependence of the wave velocity, can be converted to a one-dimensional (1-D) velocity [(shear wave (S-wave)] structure. Earlier work (e.g., Takeuchi et al. 1959, Dorman et al. 1960) demonstrated the general Lid/LVZ pattern in the ocean. The lateral variation of the oceanic LAS was also studied in the 1970s, and it was shown that the Lid thickens with age (e.g., Leeds et al. 1974, Forsyth 1975, Yoshii et al. 1976). Recent tomographic studies further confirm this plate evolution scenario (e.g., Ritzwoller et al. 2004, Maggi et al. 2006b).

The EM field is mostly sensitive to the structure just beneath the station, and station distribution is quite sparse in oceanic regions (Kelbert et al. 2014). Thus, global EM imaging can resolve only large and deep structures, but the upper mantle is imaged as a nearly uniform resistive layer with conductivity of about 0.01 S/m, which increases in the transition zone by about one order of magnitude. More detailed electrical signatures of the oceanic LAS will need to be explored by seafloor in-situ measurements.

2.1. One-Dimensional Structure

One-dimensional average properties of the oceanic LAS have been studied using various seismological approaches. These studies characterize representative structures of the LAS in the ocean.

2.1.1. Surface-wave studies. **Figure 2*a*,*b*** shows averaged S-wave velocity structures in the Pacific Ocean in the absence of abnormal topography based on two recent tomographic models as a function of plate age (Priestley & McKenzie 2013). The Lid/LVZ pattern and the general increase of S-wave velocity with plate age are evident (although the absolute values do not agree). Priestley & McKenzie (2006, 2013) used this type of information to estimate S-wave velocity as a function of temperature and pressure for given depths, reporting that S-wave velocity decreases nonlinearly when approaching the melting temperature. It is worth noting that the peak (velocity minimum) depth of the LVZ stays shallower than ~150 km. It should also be noted that **Figure 2** starts from a depth of 50 km, above which long-period surface waves cannot constrain the structure, and that surface waves have a limited sensitivity to the sharpness of velocity changes with depth: A gradual velocity decrease over ~50 km and a sharp one at the center of transition cannot be distinguished.

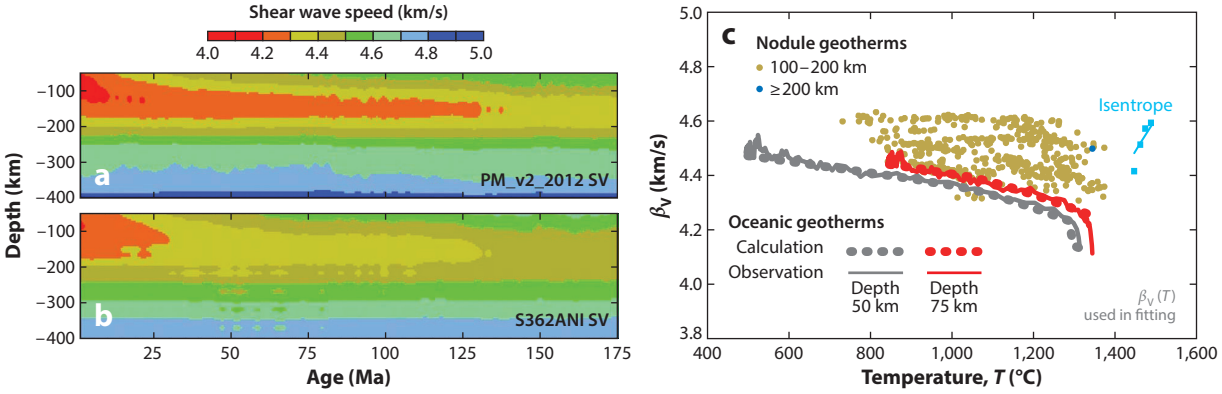

Figure 2

Shear wave (S-wave) velocity (β_V) profiles from tomographic models of the Pacific Ocean, stacked as functions of age. [Models are from (*a*) Priestley & McKenzie (2013), (*b*) Kustowski et al. (2008).] (*c*) β_V as a function of temperature estimated from panel *a*. The solid gray line shows the velocities at a depth of 50 km and the solid red line those at 75 km. All panels adapted from Priestley & McKenzie (2013) with permission.

2.1.2. Body-wave studies. To discuss the details of the LAS, information obtained by surface waves that traverse the LAS horizontally needs to be supplemented by results for body waves that traverse the LAS near-vertically.

2.1.2.1. ScS reverberation analysis. The ScS reverberation technique developed by Revenaugh & Jordan (1991) utilizes ScS-waves, which are emitted downward from earthquake sources and reflected at the core–mantle boundary. For large earthquakes, multiply reflected ScS-waves are well observed at a period longer than ∼30 s and give tight constraints on the average structure of the mantle. When seismic discontinuities, such as the 410-km or the 660-km discontinuity, are present, reflections from these discontinuities are also well observed between multiple ScS phases, giving a unique constraint on the depth and size of the impedance contrast across the boundaries. Using this technique, Revenaugh & Jordan (1991) reported the presence of a sharp ($\lesssim$40-km) velocity reduction around a depth interval of 50–100 km in the oceanic region and named it the G-discontinuity, which separates the Lid and LVZ. Although this technique provides unique and tight constraints on the nature of the LAS, a recent report from the same group (Bagley & Revenaugh 2008) substantially revised the original depth estimates for some of the paths (Bagley & Revenaugh 2008, Bagley et al. 2009, Fischer 2015).

2.1.2.2. Multiple S-wave transect. Besides ScS, multiply reflected S-waves, such as SS, SSS, SSSS, etc., pass through the LAS with slightly different incidence angles and can be used to constrain the LAS structure, as well as the velocity structure of the entire upper mantle. Tan & Helmberger (2007) analyzed waveforms of Tonga–Fiji events recorded in southern California to develop a path-averaged upper-mantle shear velocity model across the Pacific Ocean (**Figure 3**), obtaining a model that contains a fast Lid ($V_{SH} = 4.78$ km/s, $V_{SV} = 4.58$ km/s) with a thickness of 60 km. It should be noted that in this type of analysis, there is a trade-off between Lid thickness and average Lid velocity, and that the same data can be equally fitted with a 40-km-thick (or 80-km-thick) Lid with faster (or slower) velocity (see inset of **Figure 3*a***). Similar earlier attempts (e.g., by Gaherty et al. 1999) presumably suffer from the trade-off, as the imposed constraint on G-discontinuity by the ScS reverberation is now reported to be ill-constrained (Bagley & Revenaugh 2008, Fischer 2015). Constraining the depth (and the degree of velocity reduction) of the G-discontinuity is important in characterizing the LAS, as we discuss later. In the model of Tan & Helmberger (2007), the underlying LVZ is prominent, with the lowest velocities, $V_{SH} = 4.34$ km/s and $V_{SV} = 4.22$ km/s, occurring at a depth of 160 km, which is similar to the aforementioned surface-wave results. This type of data can also constrain deeper structure, such as the positive gradient below the LVZ peak, which may be useful to compare with theoretical predictions (e.g., Stixrude & Lithgow-Bertelloni 2005).

2.1.2.3. SS-precursor analysis. Teleseismic SS phases are often preceded by small-amplitude phases that correspond to their underside reflections at mantle discontinuities, which are called SS precursors. Because of their small amplitude, it is common to stack a large number of waveforms reflected from a given area in order to observe the phase. These precursors are useful in measuring the depth of discontinuity and the strength of velocity change there (e.g., Gu et al. 2001, Deuss & Woodhouse 2002), but if a reflector is too close to the surface, the time separation between SS and its precursor becomes too small to be easily detected. To avoid this difficulty, Rychert & Shearer (2011) directly modeled long-period (>10-s) SS waveforms, including both the parent SS phase and its precursor, for detecting a velocity reduction with depth in the LAS (possibly the G-discontinuity) beneath the Pacific Ocean; they reported detection of a discontinuity (sharper than ∼30 km) in some places (not in the whole Pacific Ocean) whose depth varies from 25 to 130 km

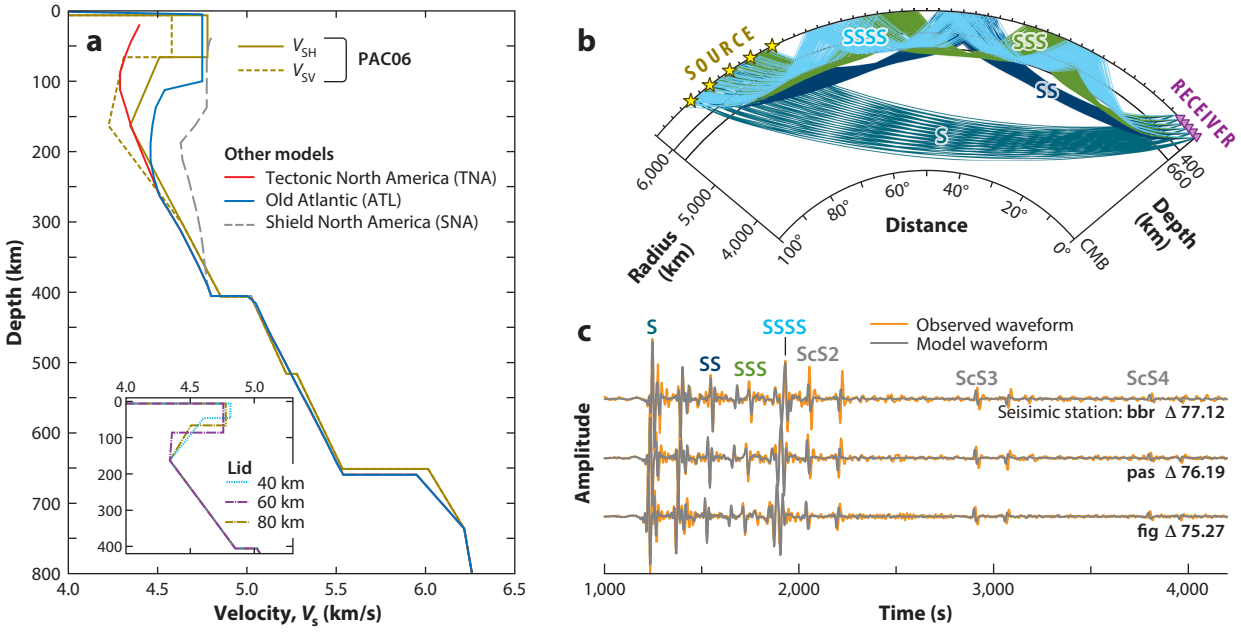

Figure 3

(*a*) Model PAC06 constructed from various S multiples—S, SS, SSS, SSSS—whose ray paths are shown in panel *b*. V_{SH} and V_{SV} used here should be taken as S-wave velocities of SH- and SV-waves, which traverse the mantle with intermediate incidence angles (i.e., these quantities are distinct from β_H and β_V). For further details on notation, see Section 2.2.1. (*Inset*) Trade-off between Lid thickness and velocity. Three models, with 40-km-, 60-km-, and 80-km-thick Lids, give a similar fit to observations. (*c*) Comparison of observed and model waveforms at three stations, whose station codes and epicentral distances are indicated. Abbreviation: CMB, core–mantle boundary. Figure adapted from Tan & Helmberger (2007) with permission.

(25 to 93 km for normal oceanic areas). A clear dependence on crustal age is evident, especially for normal oceanic areas. Schmerr (2012), using a similar dataset but differentiating seismograms in time to enhance higher-frequency content sensitive to subtle changes, directly identified phases originating from discontinuities in a depth range of 40–75 km. As the detection was limited in regions associated with recent surface volcanism and mantle melt production, Schmerr (2012) suggested that his observation is consistent with an intermittent layer of asthenospheric partial melt residing at the lithospheric base. His observation shows a very weak age dependence, and at younger ages (<20 Ma) depths are mostly deeper than 50 km, which may be due to the difficulty of separating precursors from the parent SS phase. Reported velocity reductions range from ~7% to 12%. Tonegawa & Helffrich (2012) reported detection of precursors of the sS phase (not the SS phase) originating from deep earthquakes, moving upward, and being reflected at the G-discontinuity beneath the Philippine Sea Plate (20–40 Ma). They conclude that there is a minimum S-wave contrast of −5.8% and a depth range of 50–70 km.

2.2. Seismic Anisotropy

Seismic anisotropy plays an essential role in the elucidation of the LAS. This is because plate motion–related shear motion in the asthenosphere is expected to introduce lattice-preferred orientation (LPO) of olivine, which is highly anisotropic and the most abundant mineral in the mantle (e.g., Mainprice 2015), resulting in macroscopic seismic anisotropy observable by long-period

LPO: lattice-preferred orientation

seismic waves. Although the most general form of seismic anisotropy can be described by 21 elastic constants, as opposed to two elastic constants for the isotropic case, it is common and practical to reduce the number to make the problem more tractable. The most common method is to assume axial (i.e., hexagonal) symmetry. Hexagonal symmetry requires five elastic constants in addition to the direction of the symmetry axis, and it is also called transverse isotropy (TI). When the symmetry axis is vertical (radial), such anisotropy is called radial anisotropy or TI with a vertical symmetry axis (VTI), and the standard Earth model PREM (Dziewonski & Anderson 1981) has a layer of radial anisotropy between depths of 24.4 km and 220 km. When the symmetry axis is in the horizontal plane, azimuthally varying wave propagation velocity is realized as azimuthal anisotropy.

2.2.1. Radial Anisotropy. The presence of radial anisotropy in the upper mantle is inferred from observed phase velocities of Love and Rayleigh waves that cannot be explained by a single 1-D isotropic model (Love–Rayleigh wave discrepancy). A Love wave is mainly sensitive to $\beta_H = \sqrt{N/\rho}$, the phase velocity of a horizontally polarized horizontally propagating S-wave, whereas a Rayleigh wave is sensitive to $\beta_V = \sqrt{L/\rho}$, the phase velocity of a vertically polarized horizontally propagating S-wave, where L, N, and ρ are Love's representative elastic shear moduli and the density.[1] In a radially anisotropic system, a vertically traveling S-wave has a phase velocity β_V. In the oceanic regions, $\beta_H > \beta_V$ is generally observed in the upper mantle (Forsyth 1975, Schlue & Knopoff 1977, Lévêque & Cara 1985, Nishimura & Forsyth 1989). Recent tomographic models of radial anisotropy indicate strong and laterally varying radial anisotropy in the LVZ (Ekström & Dziewonski 1998, Nettles & Dziewonski 2008, Kustowski et al. 2008). Strong and puzzling radial anisotropy (larger than 5%) is observed in the central Pacific Ocean in the LVZ. **Figure 4** shows

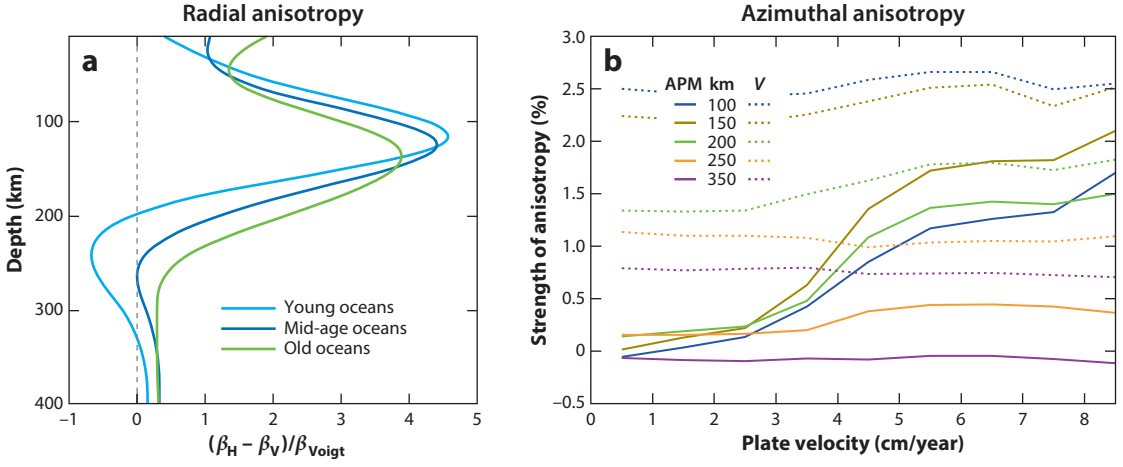

Figure 4

Strength of radial and azimuthal anisotropy. (*a*) Average radial anisotropy profiles for the oceanic regions. Panel *a* adapted from Nettles & Dziewonski (2008) with permission. (*b*) The peak-to-peak strength of azimuthal anisotropy at various depths as a function of plate velocity (*dotted lines*) and its projection onto the absolute plate motion direction (APM) (*solid lines*). Panel *b* adapted from Debayle & Ricard (2013) with permission. Note that the peak strength of anisotropy is ~4% (radial) and ~2.5% (azimuthal) for these models.

[1]The notation of S-wave velocity in a radially anisotropic system can be confusingly unclear if one fails to consider the incidence-angle dependence of body-wave velocities (Kawakatsu 2016). Here we distinguish between β_H/β_V and V_{SH}/V_{SV}; the former are as defined above, whereas the latter are wave velocities of SH/SV-waves, defined by the conventions of seismology (e.g., Aki & Richards 2002), that traverse media with arbitrary incidence angles. (The polarization of an SH-wave is horizontal, and that of an SV-wave is perpendicular to SH).

average depth profiles for oceanic areas. It is interesting to note that the peak of radial anisotropy is generally above 150 km, a depth that is comparable to the peak depth of the LVZ, and thus it seems that the strong radial anisotropy is mainly due to the strong low velocity of β_V.

2.2.2. Azimuthal anisotropy. The presence of azimuthal anisotropy in the ocean was established via refraction surveys of Pn-waves in very early studies of P-waves (e.g., Raitt et al. 1969), and also via regionalized surface-wave studies for the deeper mantle for S-waves (e.g., Forsyth 1975, Montagner 1985, Nishimura & Forsyth 1989). Tanimoto & Anderson (1984) first presented the global tomography model that inferred the connection with large-scale flow in the mantle. The growing volume of digital waveform data in the past few decades has made it possible to construct detailed tomographic models of the upper mantle (e.g., Smith et al. 2004, Ritzwoller et al. 2004, Maggi et al. 2006a, Debayle & Ricard 2013, Schaeffer & Lebedev 2013, Burgos et al. 2014), and comparison with parameters related to plate tectonics has become possible. For example, Debayle & Ricard (2013) showed that beneath fast-moving (>5 cm/year) plates (i.e., the Indian, Cocos, Nazca, Australian, Philippine Sea, and Pacific plates), between depths of 100–200 km, fast azimuthal directions generally coincide with present-day plate motion (**Figure 4**). However, for the shallow lithosphere, a better correlation is obtained with fossil accretion directions, indicating frozen-in anisotropy for the origin of lithospheric azimuthal anisotropy. From a similar comparison, Becker et al. (2014) conclude that LPO inferred from mantle flow computations produces a better fit than simple plate motion directions. In both results, it is interesting to note that the best correlation is obtained for a depth range of 150–200 km, generally deeper than the peak depth of radial anisotropy.

2.2.2.1. Limitations of surface-wave tomography. Although surface-wave tomography offers a powerful way to constrain the structure of the uppermost mantle, it is important to recognize that there are certain limitations, especially for the elucidation of the oceanic LAS. First, the difficulty of measuring short-period surface-wave dispersions (which is caused by multipathing that results from shallow lateral heterogeneities) makes the structure above ∼50 km undetermined, and thus it is common to assume some structure, including sediment and crustal structures. It is known that there is a trade-off between the shallow structure and the deeper structure, especially in radial anisotropy at depths of ∼100 km (Bozdağ & Trampert 2008, Ferreira et al. 2010). Second, the relative strength of radial and azimuthal anisotropy, which gives an essential constraint on the origin of anisotropy, is difficult to constrain because of the nonuniqueness of damping parameters inherent in inversion methods (e.g., Smith et al. 2004). Third, the depth resolution is limited to ∼50 km and therefore prevents detailed investigations of the origins of peculiar structures, such as the G-discontinuity. In light of these limitations, the usage of depth derivatives of various tomographic models should be treated carefully unless high-resolution regional modeling is conducted (e.g., Yoshizawa 2014).

2.2.2.2. Subslab anisotropy. Change of the dip of the LAS at a subduction zone provides a unique way to investigate the anisotropy of the LAS. Radial anisotropy in the LAS under the oceanic environment is difficult to observe using shear-wave splitting, as nearly vertically incident S-waves, such as SKS-waves, are not sensitive to radial anisotropy. Song & Kawakatsu (2012) have demonstrated that strong radial anisotropy of the suboceanic LAS observed by surface-wave tomography (e.g., Kustowski et al. 2008) (**Figure 4**) can have a significant effect on the observed SKS-wave splitting when the system is dipping, as in subduction zones, and that this might well explain the so-called subslab trench-parallel fast directions at the majority of subduction zones (Long & Silver 2008) without invoking any unrealistic trench-parallel flow in the mantle. When

azimuthal anisotropy present in the suboceanic LAS is incorporated in the modeling, they further showed that trench-normal fast directions at shallowly dipping subduction zones, such as the Cascadia subduction zone and the central South American subduction zone, can also be explained by a single model of orthorhombic anisotropy; if this model represents the general property of suboceanic anisotropy, radial anisotropy is stronger (~3–4%) than azimuthal anisotropy (~2%) (**Figure 4**); thus, it may require modification of the commonly accepted view that the A-type olivine fabric (Jung et al. 2006) is the dominant one in LAS, implying rather that the AG-type fabric (Mainprice 2015) is dominant (Song & Kawakatsu 2013).

BBOBS: broadband ocean-bottom seismometer

3. CONSTRAINT FROM SEAFLOOR OBSERVATIONS

3.1. Active Source (Pn)

The crustal structure and the uppermost mantle just below the Mohorovičić discontinuity (Moho) have been extensively studied by active-source seismic surveys in the ocean (e.g., Raitt et al. 1969, White et al. 1992, Shinohara et al. 2008). A recent, interesting finding is that the strength of Pn azimuthal anisotropy can be expressed as a linear function of the ancient spreading rate at the ridge (Song & Kim 2011), indicating that the origin of the anisotropy is directly related to the spreading process. The direction of the fast axis is generally believed to be perpendicular to the spreading axis, but Toomey et al. (2007) reported a 10° rotation from the plate-spreading direction and Gaherty et al. (2004) also reported such a possibility. Takeo et al. (2016) also reported a rotation angle of more than 50° for the S-wave fast direction (**Figure 5*d***).

Studies beyond the sub-Moho depth range in the oceanic lithosphere (Lid) are quite limited. The Lid structure is often assumed to be nearly constant with depth (e.g., Gaherty et al. 1999, Tan & Helmberger 2007, Shinohara et al. 2008), but the structure has never been seriously examined. The refraction survey by Lizarralde et al. (2004) reported that the P-wave velocity structure beneath the mid-ocean-ridge region in the northern Atlantic Ocean increases with depth at the top of the mantle, an observation that is contrary to the theoretical prediction for the pyrolytic composition, with temperature and pressure effects that predict a steep decrease of velocity with depth. Recent direct measurements using broadband ocean-bottom seismometer (BBOBS) data also support such a Lid-like velocity structure in the Philippine Sea (Takeo et al. 2013; see also **Figure 5*b***). Regarding azimuthal anisotropy, Shimamura et al. (1983) reported the presence of extremely large (~13%) values in the deeper part of the Lid in the northwestern Pacific Ocean, but recent BBOBS observations so far do not confirm such a strong azimuthal S-wave anisotropy in the deeper part of the oceanic Lid (e.g., Takeo et al. 2016). The deeply penetrating P-wave observation of Shimamura et al. (1983) (due to the long-distance traveling of P-waves) should probably be understood in terms of the scattered wavefield that will be discussed later, but the enigma of the strong anisotropy is yet to be resolved.

3.2. Broadband Dispersion Analysis

Advances in array-based analysis techniques in seismology, together with advances in broadband ocean-bottom seismometry (Suetsugu & Shiobara 2014), have brought great opportunities for resolving the structure of the LAS in the ocean. Array methods for surface-wave analysis consist of two components: ambient noise cross-correlation and teleseismic event analysis. The former utilizes continuous recordings of the ambient noise seismic wavefield to extract waves traveling between pairs of stations at ~10-s periods, and has become a powerful way to resolve the shallow subsurface structure on land (Aki 1957, Shapiro et al. 2005, Nishida et al. 2008). The latter analyzes

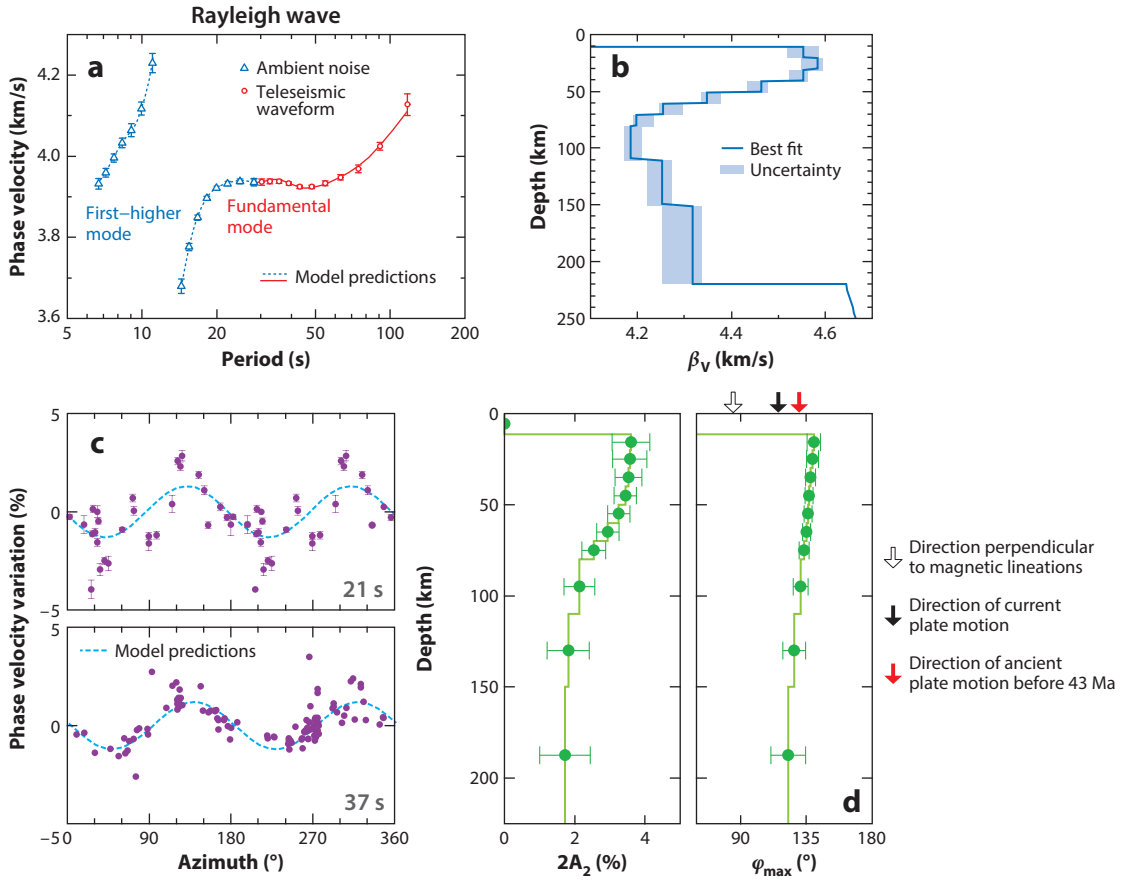

Figure 5

Broadband dispersion analysis. (*a*) Phase velocities of Rayleigh waves in the Philippine Sea region (20 Ma) measured by ambient noise cross-correlation (*blue triangles*) and teleseismic waveform array analysis (*red circles*). Solid and broken lines are model predictions. (*b*) 1-D S-wave (β_V) structure model (at 1 Hz) that explains the observations in panel *a*; it has much better depth resolution compared to global tomography. Panels *a* and *b* adapted from Takeo et al. (2013) with permission. (*c*) Azimuth-dependent phase velocity measurements of Rayleigh waves at two different periods in the French Polynesian region (60 Ma). Circles denote measurements, and broken lines denote model predictions. (*d*) Modeled depth profiles of the strength of azimuthal anisotropy (*left*) and the fast direction (*right*). Panels *c* and *d* adapted from Takeo et al. (2016) with permission.

teleseismic surface waves to extract a coherent signal within an array by evaluating ray bending and multipathing of short-period (but longer-period than ambient noise) surface waves (Forsyth & Li 2005). By combining the two, broadband dispersion and tomographic analyses, including anisotropy, have become possible (e.g., Lin et al. 2010).

In the ocean, extensive analyses have been conducted across the East Pacific Rise (EPR) region (e.g., Dunn & Forsyth 2003, Forsyth & Li 2005, Weeraratne et al. 2007, Harmon et al. 2007). Harmon et al. (2007) first applied the ambient noise correlation method for ocean-bottom seismometer (OBS) records and, by measuring dispersion of Rayleigh waves, obtained a 1-D structure of β_V from the crust to a depth of ~100 km with a depth resolution much higher than that of global tomography. Weeraratne et al. (2007) reported the measurement of azimuthal anisotropy

EPR: East Pacific Rise

OBS: ocean-bottom seismometer

RF: receiver function

of fundamental-mode Rayleigh waves. By analyzing records of BBOBSs previously deployed in the Philippine Sea region, Takeo et al. (2013) reported the broadband dispersion measurement of both Rayleigh and Love waves from a period range of 3–100 s and constructed an average 1-D radially anisotropic structure from the crust to the asthenosphere depth range for the Shikoku Basin, whose crustal age is ∼20 Ma (**Figure 5**). Takeo et al. (2016) conducted a similar broadband dispersion analysis (5–200 s) for the BBOBS array deployed in the French Polynesian region (∼60 Ma) and measured the dispersion of fundamental-mode and first higher-mode Rayleigh waves, including azimuthal anisotropy; the model thus obtained shows a peak-to-peak intensity of azimuthal anisotropy of 2–4% that decreases with depth, with the fastest azimuth in the NW-SE direction (rotated more than 50° from the perpendicular direction of the magnetic lineations) in both the lithosphere and the asthenosphere, suggesting that the ancient flow frozen in the lithosphere is not perpendicular to the strike of the ancient mid-ocean ridge but is roughly parallel to the ancient plate motion.

Note that it is challenging to measure Love wave dispersion in the ocean. Depending on the nature of the Lid-LVZ structure, the Love wave fundamental mode and higher modes possess similar group velocities and interfere with each other, making dispersion measurement extremely difficult in a period range of ∼10–50 s. This is especially true in the ocean, as has been known for some time (e.g., Nettles & Dziewoński 2011), and may severely affect small-aperture-array observations of Love wave dispersion (and thus radial anisotropy estimation) (Foster et al. 2014, Takeo et al. 2016).

3.3. Receiver Function Analysis

The receiver function (RF) analysis method utilizes P-to-S or S-to-P conversion phases to characterize a sharp S-wave velocity change beneath a seismic station. Whereas application of this method to expore discontinuities in the continental mantle has been very common (e.g., Fischer 2015), its use for the oceanic LAS has been limited. This is because OBSs generally have large noise in the horizontal components, which RF analysis requires; also, strong reverberation phases in the water layer (appearing in the vertical component) and sediment layer (in the horizontal component) make modeling and interpretation of RFs for subsurface structure extremely difficult (e.g., Audet 2016). To reduce these difficulties, Japanese researchers constructed seafloor borehole seismic stations in the Philippine Sea and northwestern Pacific Ocean; broadband seismic sensors were deployed in two deep boreholes below the sediment layer, enabling high-quality observation for a limited time period (Shinohara et al. 2008). Employing both P-RF and S-RF methods for data from these stations, Kawakatsu et al. (2009) and Kumar et al. (2011) reported observation of sharp discontinuities (i.e., G-discontinuities) in the mantle, which they interpreted as signatures characterizing the LAB. Kawakatsu et al. (2009) also suggested that the observed S-velocity reduction (7–8%) might be explained by the presence of shear-induced banded melt zones (Holtzman et al. 2003) in the asthenosphere—named the millefeuille asthenosphere[2]—that should contribute to the reported radial anisotropy there (e.g., Ekström & Dziewonski 1998, Nettles & Dziewonski 2008). RF analysis using conventional pop-up type (BB)OBSs to resolve shallow mantle structure remains highly challenging, but there are some recent developments that may become useful (e.g., Audet 2016, Akuhara et al. 2016).

[2]The millefeuille model is often misunderstood, as it requires a melt fraction of 0.25–1.25% (e.g., Hirschmann 2010), but mathematically speaking the melt fraction can be much lower.

3.4. Seismic Scatterers/Small-Scale Heterogeneities

Although the detailed velocity structure of the oceanic lithosphere (Lid) is not well constrained, recent analyses of BBOBS data indicate clear evidence for a peculiar scattering property of the oceanic lithosphere that sheds new light on the origin and formation mechanism of the lithosphere. By analyzing BBOBS recordings of deep-focus earthquakes occurring in the subducting slab beneath Japan, Shito et al. (2013) reported the presence of large-amplitude, high-frequency, long-duration coda waves for both P- and S-waves that were previously known as Po- and So-waves (or sometimes just called Pn/Sn) (e.g., Walker 1977). Combining this observation of Po- and So-waves with finite-difference wave propagation simulation analysis (Furumura & Kennett 2005), Shito et al. (2013) demonstrated that Po/So-waves are generated by scattering due to laterally elongated heterogeneities in both the subducting and horizontal parts of the oceanic lithosphere (**Figure 6**). Subsequent analyses (Shito et al. 2015, Kennett & Furumura 2013, Kennett et al. 2014) indicated that such scatterers exist in parts of the lithosphere as young as ∼15 Ma, but Po/So-waves propagate much more efficiently in the older lithosphere, suggesting that the creation of those scatterers may be directly linked to the generation and/or growth of the oceanic lithosphere.

The seismological observations so far are all compatible with quasi-laminate features with a horizontal correlation length of 10–50 km and a vertical correlation length of 0.5 km, with a uniform level of about ∼2% variation through the full thickness of the lithosphere. Kennett & Furumura (2015), however, suggest that models with stronger heterogeneity near the base of the lithosphere, or even in the asthenosphere, might equally explain the observations, although there remains a need for some quasi-laminate structure throughout the mantle component of the oceanic lithosphere. They suggest that these models are more compatible with petrological models (e.g., Hirschmann 2010, Tommasi & Ishikawa 2014), which might favor stronger heterogeneity at the base of the lithosphere associated with underplating from frozen melts. Recent active-source surveys also report observations of scatterers in the deeper part of the lithosphere (e.g., Kaneda et al. 2010), and the stochastic nature of Po/So-wave observations might be investigated deterministically via ocean-bottom observations in the future.

3.5. Seismic Attenuation

Seismic attenuation is the least constrained physical parameter, both from the observational and from the theoretical/experimental point of view. From the former, it is quite challenging to separate intrinsic (anelastic) and extrinsic (scattering, heterogeneity) attenuation effects from waveform data, resulting in very different views for the cause of attenuation (intrinsic is thermally activated, whereas extrinsic is a structural effect); from the latter, the physical conditions of laboratory experiments are limited, and interpolations and extrapolations are required for making inferences for the mantle conditions (e.g., Jackson et al. 2014, Takei et al. 2014). Nevertheless, we summarize the relevant observations. Dalton et al. (2009) performed a global tomographic study of upper mantle attenuation and showed general strong (anti)correlation between attenuation and velocity (strong attenuation correlates well with low velocity). From local observations in oceanic areas, employing the array technique of Forsyth & Li (2005), Yang et al. (2007) studied seismic attenuation near the EPR region (2-Ma and 6-Ma areas) and suggested, with empirically determined scaling between attenuation and velocity, the presence of a melt beneath or near the ridge between a depth range of 25–40 km and ∼100 km. Recent observation of the old seafloor of the western Pacific Ocean (150–160 Ma) exhibits attenuation in the depth range of the LVZ as strong as that observed at the EPR (**Figure 7**), suggesting the presence of small fractions of melt in the asthenosphere of the oldest part of the Pacific Ocean; note that the observational constraint for attenuation is the combined effects of intrinsic and extrinsic attenuation (Booth et al. 2014).

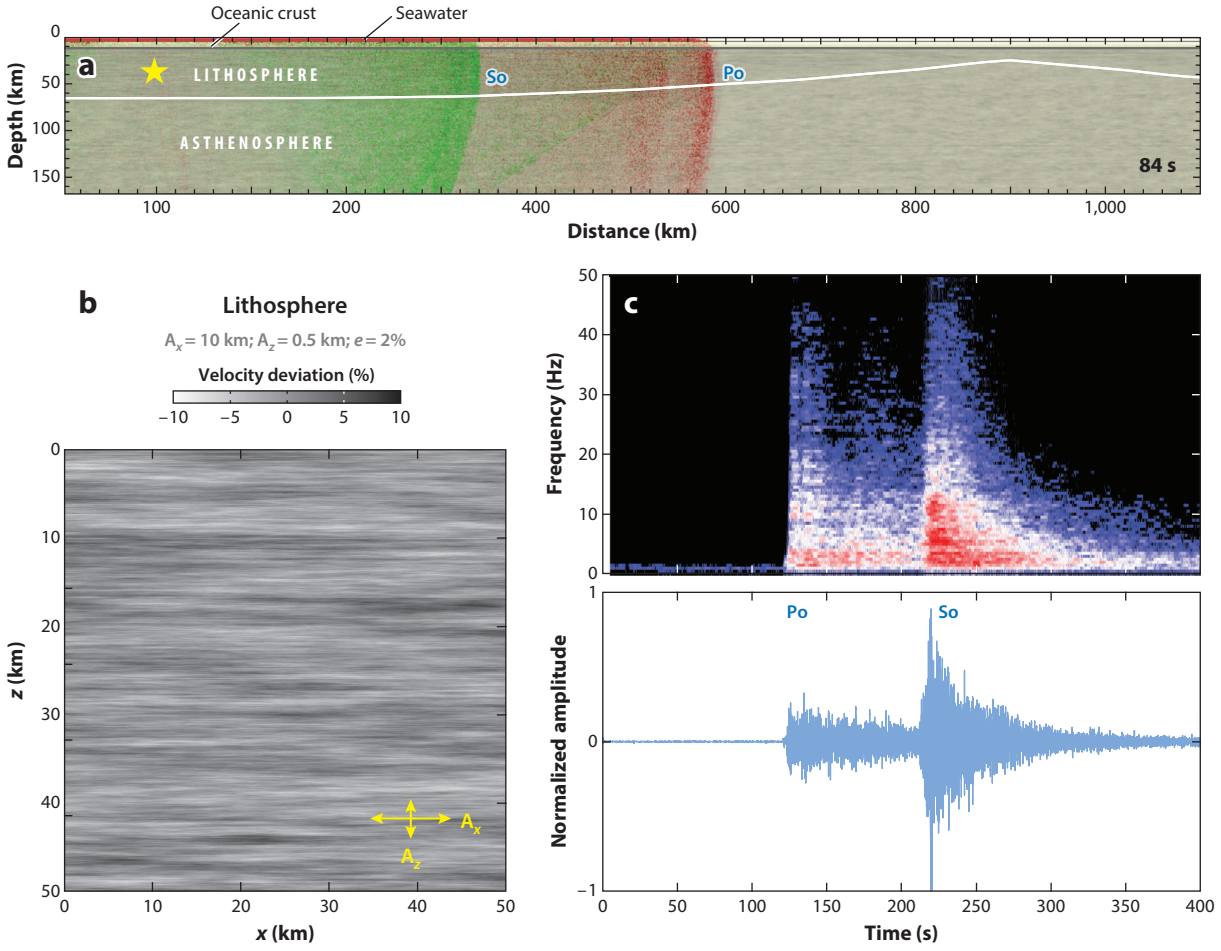

Figure 6

Po/So: (*a*) Snapshots of the seismic wavefields calculated for a 2-D model of the lithosphere–asthenosphere system with laminar scatterers shown in panel *b*. (*b*) Representation of the stochastic scatterers model for the lithosphere. Horizontal (A_x) and vertical (A_z) correlation lengths are 10 km and 0.5 km, respectively, and the strength of velocity perturbations, *e*, is 2%. Panels *a* and *b* courtesy of T. Furumura. (*c*) Observation of Po- and So-waves: running spectra (*top*) of a vertical velocity waveform (*bottom*). Panel *c* adapted from Shito et al. (2013) with permission.

3.6. Seafloor Magnetotellurics

The magnetotelluric (MT) method is one of the EM methods used to explore the electrical conductivity structures within Earth's interior, based on the correlation between electric and magnetic field fluctuations simultaneously observed at a site. The application of the method at the bottom of the deep ocean had been a technological challenge until a few decades ago.

MT: magnetotelluric

OBEM: ocean-bottom electromagnetometer

3.6.1. High-conductivity layer ≈ electrical asthenosphere. Because of the difficulty of using global EM approaches to study shallower parts of the mantle, seafloor magnetotelluric array studies using ocean-bottom electromagnetometers (OBEMs) are regarded as the only practical approach for EM exploration of the oceanic LAS. Each OBEM measures two components of electric and three components of magnetic field variations in the period range between a few hundred seconds

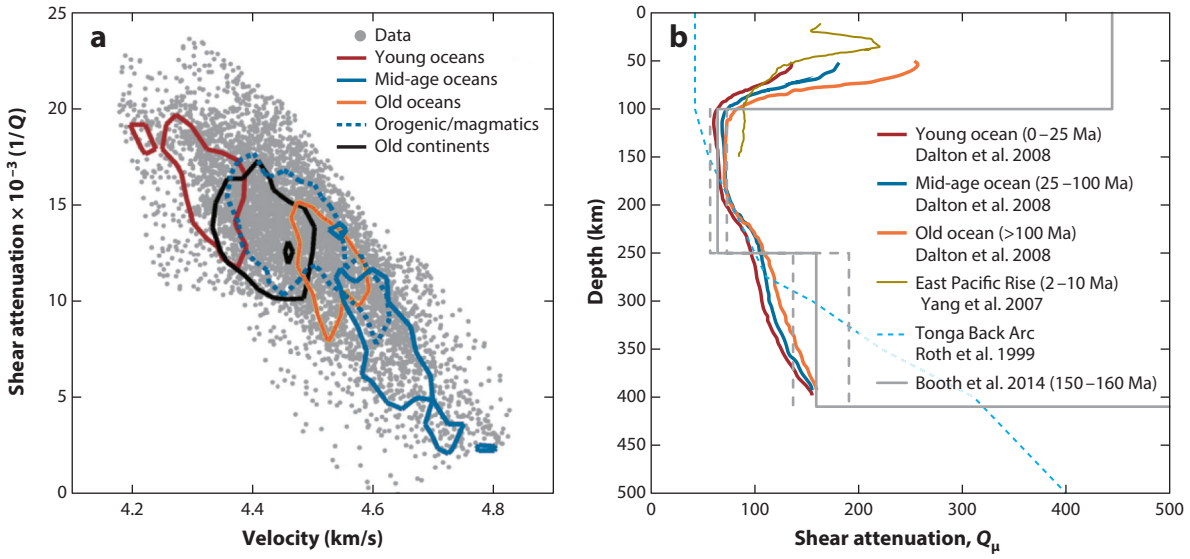

Figure 7

Seismic attenuation: (*a*) Scatter plot showing the shear velocity and shear attenuation values at a depth of 100 km. Panel *a* adapted from Dalton et al. (2009) with permission. (*b*) Shear attenuation model beneath old western Pacific seafloor (*solid gray line*; uncertainty ranges are denoted by *broken gray lines*) compared with other oceanic shear attenuation models. Panel *b* adapted from Booth et al. (2014) with permission.

and one day (Utada 2015). The depth resolution of the MT method relies on the EM skin effect: The longer the variation period is, the deeper the EM signals of external sources penetrate into the conductive Earth. As a result, seafloor MT data, especially those gathered at deep-ocean sites, are usually insensitive to the conductivity in the crust and shallower part of the upper mantle because of the strong attenuation of short-period signals through conductive seawater. However, a few controlled-source EM experiments (Cox et al. 1986, MacGregor et al. 2001, Key et al. 2012) provide solid evidence that the shallowest part of the oceanic crust is highly conductive because of the presence of sediments with saline water but that the deeper part of the oceanic lithosphere is very resistive (**Figure 8*a***). A high-frequency MT result at relatively shallow water around the EPR (Key et al. 2013) also constrains the presence of the LCL corresponding to the lithosphere.

In the case of seafloor MT data from deep-ocean sites, a model of conductivity is estimated with a priori constraints on the conductivity of the LCL (e.g., Baba et al. 2010). The EM method is more sensitive to conductive structures in general, and in fact the main structural feature of the HCL depends little on assumptions about the LCL's conductivity, as shown in **Figure 8*b***. Conductivity changes smoothly with depth from the LCL to the HCL and then becomes almost constant throughout the HCL. Here, the depth at which there is maximum curvature in this transition is used as a proxy for the depth of the HCL.

In **Figure 9*a***, HCL depths estimated from recent seafloor MT results are presented as a function of plate age. These HCL depths do not show a simple age dependence, which might be expected from a model of plate cooling. It is most likely that a simple age dependence of normal oceanic mantle is being masked by structural variation from other causes. For example, the youngest result shown in **Figure 9*a***, from the MELT (Mantle Electromagnetic and Tomography) experiment (Evans et al. 1999), shows a greater HCL depth than two results from 20–30-Ma seafloor. The two oldest (140–150-Ma) results, from the northwestern Pacific subduction zone

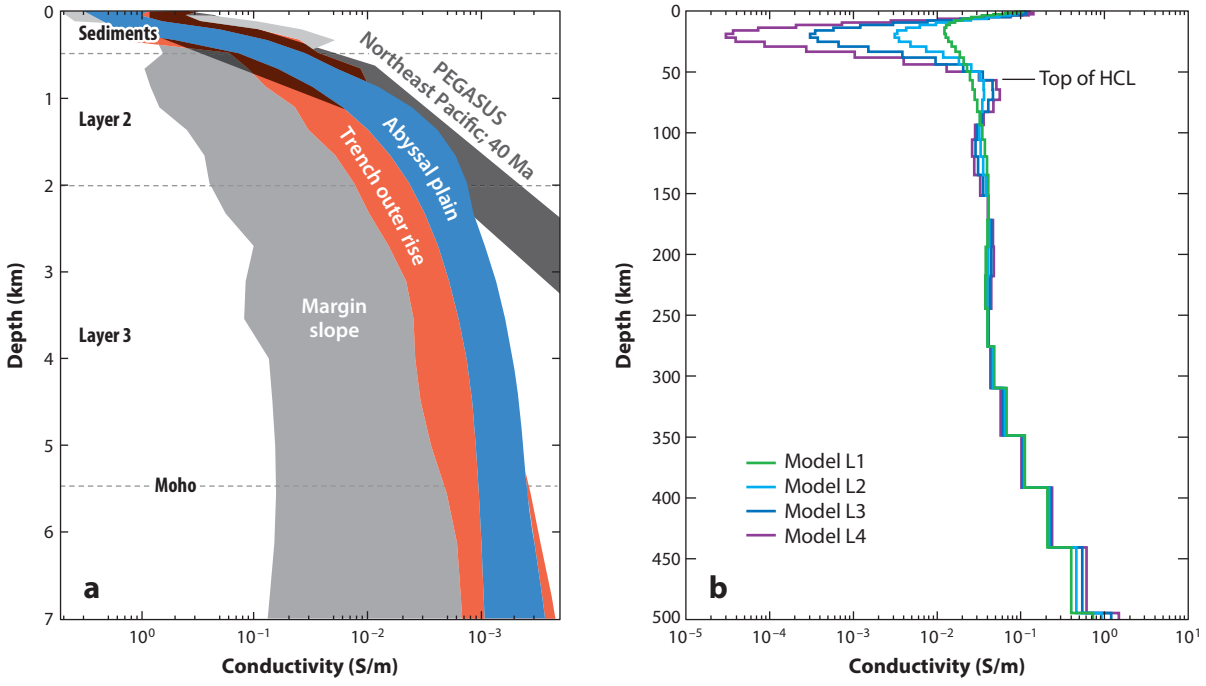

Figure 8

(*a*) 1-D conductivity profiles obtained by controlled source electromagnetic survey at abyssal plain (*blue*), trench outer rise (*red*), and margin slope (*light gray*) in the Middle America Trench offshore from Nicaragua, and from the PEGASUS experiment (*dark gray*) in the northeast Pacific. Horizontal lines show crustal layering observed by active-source seismics. Panel *a* adapted from Key et al. (2012) with permission. (*b*) 1-D profiles obtained by inversion of seafloor magnetotelluric data in the Philippine Sea with different constraints on the shallow structures. Panel *b* adapted from Baba et al. (2010) with permission. Abbreviation: HCL, high-conductivity layer.

(Baba et al. 2010), show a very deep HCL (thick LCL) of >150 km, which we discuss in Section 4. If we remove these three results, which might reflect anomalous features near plate boundaries, the dependence of the HCL depth on age appears more consistent with a plate-cooling model.

The conductivity of the HCL is another robust parameter obtained from MT data. **Figure 9*b*** shows the age dependence of the maximum conductivity values in the HCL. We notice that the conductivity of the HCL does not exhibit much age dependence, taking similar values of about −1.4 on a log scale (about 0.04 S/m). The only apparent exception is from the 23-Ma Cocos Plate off Nicaragua (Naif et al. 2013). This extremely high conductivity may be ascribed to strong shear in the asthenosphere arising from the high convergence rate (85 mm/yr) of the Cocos Plate.

3.6.2. Electrical anisotropy. MT response, usually called impedance, is a second-order complex-valued tensor usually defined in the frequency domain, relating vectors of horizontal electric and magnetic field variations. Impedance tensors determined from observations generally show anisotropic features, but this does not mean that subsurface materials are electrically anisotropic. Lateral heterogeneity of underground structure also causes apparently anisotropic impedance. For seafloor MT, bathymetric variations and coastline geometry are also possible sources of apparent anisotropy. In fact, it is generally difficult to distinguish the effects of intrinsic anisotropy from those of lateral heterogeneity.

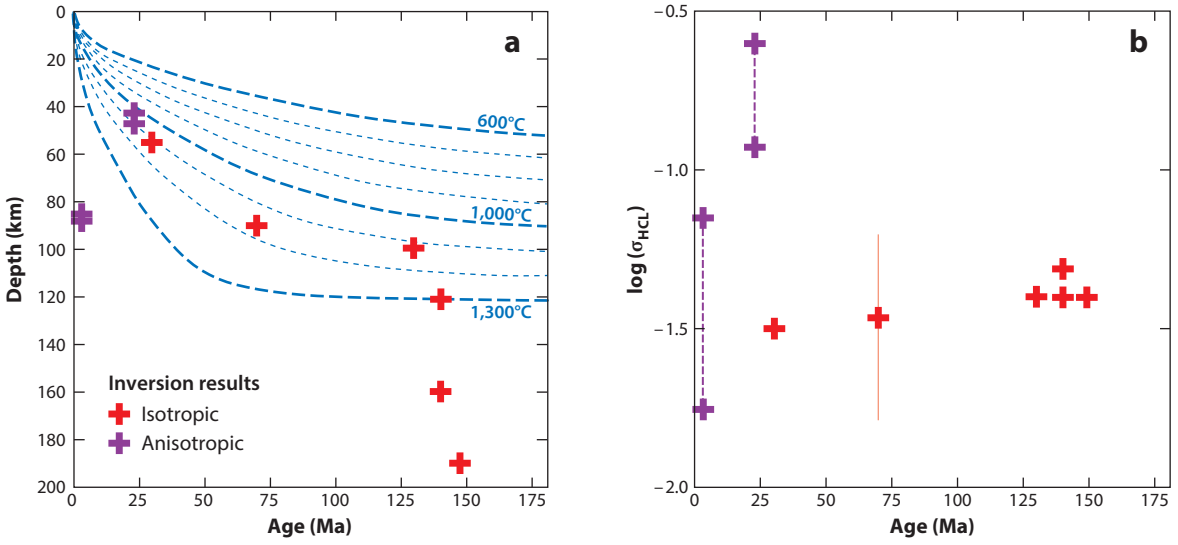

Figure 9

(*a*) Depth to the HCL (high-conductivity layer) versus seafloor age with temperature profiles by plate cooling (the constant thermal conductivity model of McKenzie et al. 2005) and (*b*) the maximum conductivity value of the HCL versus seafloor age. Red and purple symbols denote isotropic and anisotropic inversion results, respectively, and the red vertical bar indicates a range of variation.

Nevertheless, there have been a few examples of attempting anisotropic inversion for seafloor MT data. Initial results were reported from the MELT experiment conducted around the EPR (Evans et al. 2005, Baba et al. 2006). A 2-D anisotropic inversion revealed azimuthal electrical anisotropy in the HCL below the Nazca Plate with higher conductivity by nearly one order of magnitude in the direction of plate spreading, as shown in **Figure 10**. This anisotropic feature was interpreted in terms of crystallographic orientation of hydrous olivine crystals (Evans et al. 2005), which, as well as the relatively deep HCL for the plate age, is regarded as strong evidence for compositional (hydrogen content) control over the electrical conductivity of the oceanic plate.

A second example, from Naif et al. (2013), can be seen offshore from Nicaragua, where the Cocos Plate (mean seafloor age 23 Ma) is subducting below Central America. The azimuthal anisotropy was estimated, by 2-D anisotropic inversion, for both the LCL and the HCL, with the resulting contrast between high- and low-conductivity directions shown in **Figure 10**, although the anisotropy of the LCL is not well constrained by the data. The inferred contrast of a factor of about 3 is slightly weaker than the MELT result. The anisotropy in the HCL was ascribed exclusively to the presence of partially molten layers with shear deformation, because the average (isotropic) conductivity is too high to be accounted for by the effects of hydration (Naif et al. 2013, Pommier et al. 2015). Dai & Karato (2014) suggested, on the basis of their new laboratory results, that the high conductivity and anisotropy are both consistent with a hydrous asthenosphere model. According to their laboratory data, the anisotropy estimated from the MELT experiment may be slightly too intense to be accounted for by the effect of hydrogen. On the other hand, this partial melt model needs an additional mechanism to explain the anisotropy in the LCL, if it is significant.

A third example is a result from the Mariana subduction zone, where the 140–150-Ma Pacific Plate is subducting below the Philippine Sea plate (Matsuno et al. 2010). A 2-D inversion suggests the presence of the HCL at a depth of 70–100 km beneath the Pacific Plate, showing azimuthal anisotropy with a contrast of a factor of 3 between conductive (trench-normal) and resistive

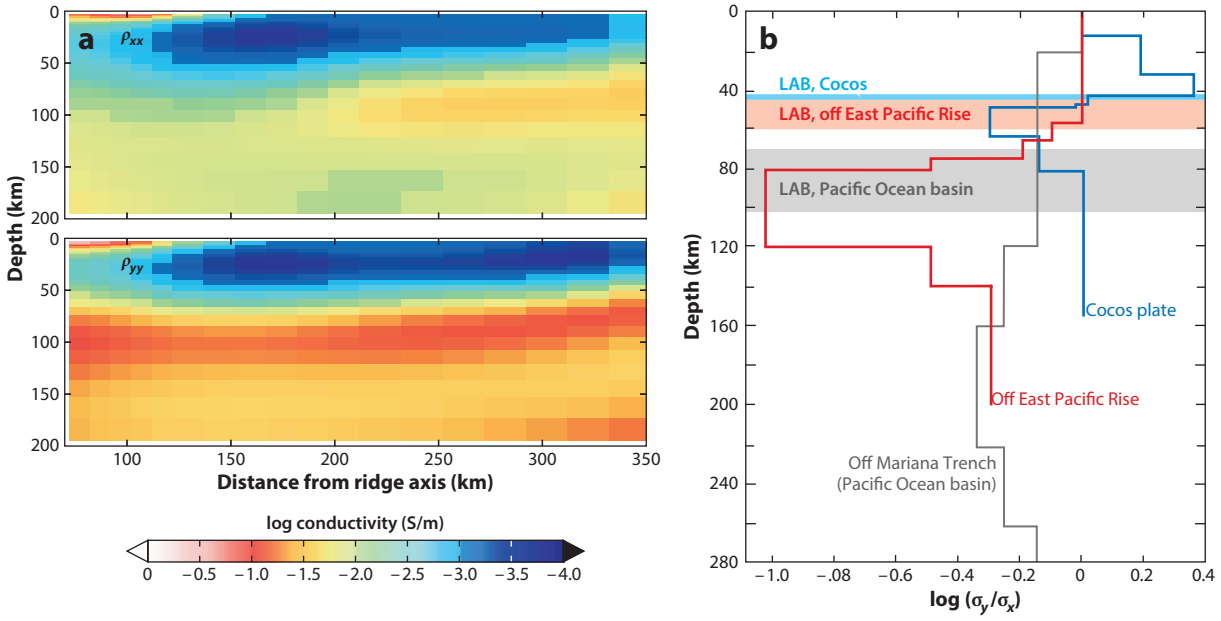

Figure 10

(*a*) Electrical anisotropy obtained from the MELT experiment (Evans et al. 2005) showing estimated conductivity values in the (*top*) ridge parallel and (*bottom*) perpendicular directions. (*b*) Anisotropic conductivity models obtained from electromagnetic data from three different regions [the Cocos Plate in *blue*, off the EPR (the MELT experiment) in *red*, and off the Mariana Trench in *gray*]. The ratio of conductivity values in conductive and resistive directions in the HCL is presented as a function of depth. Panel *b* adapted from Pommier et al. (2015) with permission. Abbreviations: EPR, East Pacific Rise; HCL, high-conductivity layer; LAB, lithosphere–asthenosphere boundary.

(trench-parallel) directions. On the back arc side, the HCL is found at shallower depths and shows a slightly weaker anisotropy of a factor of 2. These smaller values of anisotropy compared with the MELT result were ascribed to a slower flow velocity in the asthenosphere than the flow velocity below the fast-spreading ridges in the previous two cases. However, the relative motion of the Nazca Plate is about 45 mm/yr in the hot-spot coordinate frame, which is about a half of the convergence rate of the Cocos Plate and similar to the convergence rate of the old Pacific Plate in the Mariana subduction zone.

For further discussion, improvement of the data analysis method, allowing separation of the effects of lateral heterogeneity and intrinsic anisotropy in observed MT impedances, will be indispensable. To achieve this, one needs a dataset that is sensitive to both intrinsic anisotropy and lateral heterogeneity. Unfortunately, an array along a line is not sensitive to lateral variation of the structure perpendicular to the line. Observation has to be done in a 2-D array. Although there are a few seafloor EM studies with a 2-D array, separation of intrinsic anisotropy from other effects has not yet been successful (Utada 2015).

3.6.3. Bottom of asthenosphere. We have seen that the signature of the top of the asthenosphere (LAB) can be studied by seismic and EM observations. However, its bottom is not well characterized by these observations, although the thickness of the asthenosphere has a significant impact on distinguishing between flow patterns predicted by different models of the asthenosphere (e.g., Phipps-Morgan et al. 1995, French et al. 2013). It is difficult, especially for the EM method, to characterize such great depths. Recently, Matsuno et al. (2017) estimated the depth

of the bottom of the HCL beneath the northwestern Pacific Basin by long-period MT. It was inferred from the result that EM observations are compatible with the bottom of the HCL being in the depth range of 200–300 km. Although it is a preliminary result, this might indicate that the asthenosphere has a bottom within the upper mantle. The depth range inferred by this study includes that of the Lehmann discontinuity, at about 220 km, which defines the bottom of the anisotropic layer in PREM (e.g., Dziewonski & Anderson 1981). Although PREM has this structure built in it, the presence of the Lehmann discontinuity in the ocean is not widely accepted. Earlier SS-precursor studies suggested the absence or intermittent/weak presence of such a structure beneath the oceans, whereas it is better observed in the continental regions (Gu et al. 2001, Deuss & Woodhouse 2002).

4. OBSERVATIONS AT AND NEAR SUBDUCTION ZONES

Subduction zones offer a unique environment for studying the oceanic LAS, as land-based high-density network data may be directly used to map slab and subslab structures that correspond to the LAS in the oceanic environment. Using dense Japanese Hi-net data, Kawakatsu et al. (2009) obtained a clear RF image of a sharp surface of S-wave velocity reduction and suggested a connection between this and the observation of the G-discontinuity at a depth of ~80 km beneath the seafloor (**Figure 11**). S-RF imaging by Kumar & Kawakatsu (2011) used records of onshore broadband stations located along the northern Pacific Rim, and the authors reported that the

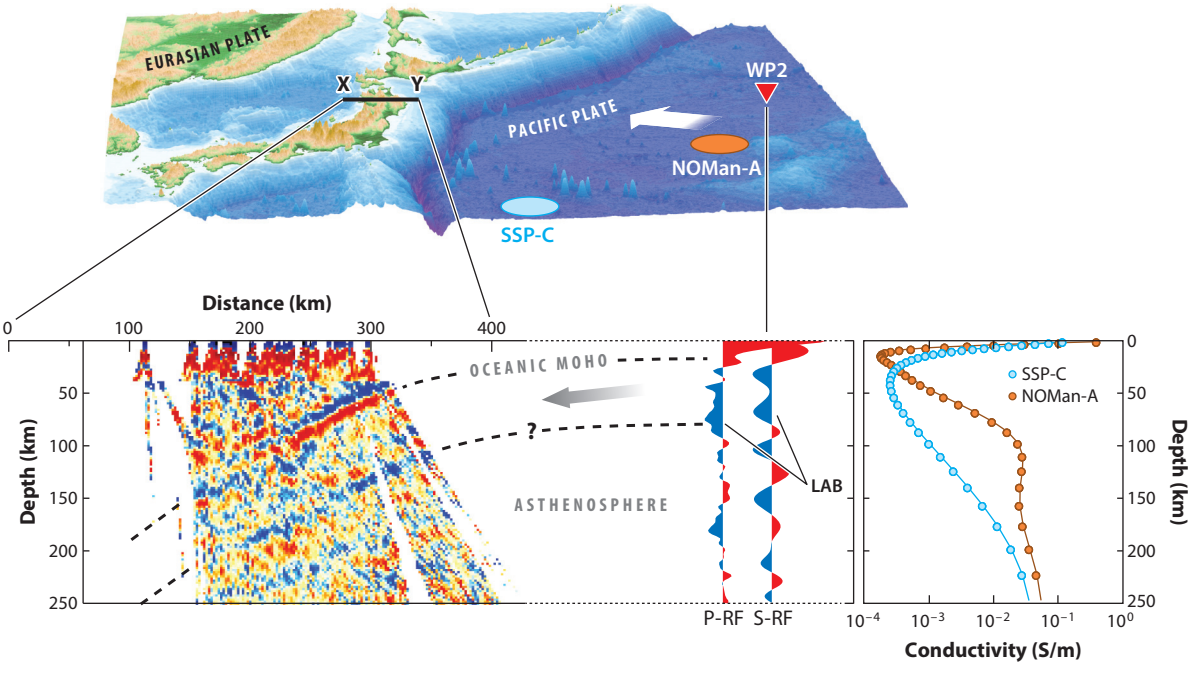

Figure 11

Lithosphere–asthenosphere system at a subduction zone: Shown are a P-RF image using dense land seismic data of Hi-net from Japan and a P-RF and S-RF image for the seafloor borehole station WP2, adapted from Kawakatsu et al. (2009). Also shown are the regional electrical conductivity profiles in two areas, NOMan-A and SSP-C; these data are from Baba et al. (2013). Abbreviations: LAB, lithosphere–asthenosphere boundary; NOMan, Normal Oceanic Mantle Project; P-RF, P-receiver function; S-RF, S-receiver function; SSP, Stagnant Slab Project.

estimated thickness of oceanic plate increased with plate age, although the data points are quite scattered.

At the Hikurangi subduction zone (120 Ma) in New Zealand, Stern et al. (2015) observed high-frequency P-wave reflectors (at thicknesses of 73 km and 83 km from the slab surface) and interpreted this 10-km-thick low-velocity (P-wave velocity reduction of 8%) layer as a low-viscosity channel at the LAB that decouples plates from the underlying mantle flow. At the Middle America Trench offshore from Nicaragua (23 Ma), Naif et al. (2013) showed that underneath the LCL, the HCL is confined to depths of 45–70 km, which they interpreted as a partially molten layer capped by an impermeable frozen lid that is the base of the lithosphere. Although these new observations appear to be finding structures near the base of the subducting lithosphere, it should be realized that a thin (~10 km) low-velocity channel is not consistent with the G-discontinuity-like structure (e.g., large velocity reduction) inferred by teleseismic body-wave analyses (e.g., Bagley & Revenaugh 2008, Kawakatsu et al. 2009, Rychert & Shearer 2011).

Figure 11 shows regional electrical conductivity profiles that indicate large lateral variation of electrical conductivity (thickening of LCL near the trench in a short distance) in the old part of the Pacific Plate (Baba et al. 2013) (**Figure 9**). According to regional 3-D inversion results (Tada et al. 2014), this extremely thick LCL does not extend further to the south, where the older (about 160 Ma) Pacific Plate is subducting beneath the Mariana arc, suggesting that the thickening of the LCL near the trench is likely to be a regional feature along the Japan–Izu–Ogasawara subduction zone. Considering that petit-spot volcanism, a recent volcanism that might be associated with the deformation of the oceanic plate before subduction (Hirano et al. 2006), is also observed in the same region, there might be a close connection between the two phenomena.

5. VIEWS OF LITHOSPHERE–ASTHENOSPHERE SYSTEM OF NORMAL OCEANIC MANTLE

For the elucidation of the LAS in the ocean, we first list the most robust observations that, we think, any modeling attempt should be able to explain. They are

1. the thermal evolution of the LAS as depicted by surface-wave tomography,
2. the presence of seismic anisotropy in the LAS,
3. the presence of the G-discontinuity,
4. the presence of lithospheric laminar heterogeneities, and
5. the presence of the LCL and HCL.

5.1. Nature of Lid/LVZ and LCL/HCL Transitions

Investigation of the LAB has been a focus of recent global geophysics/geodynamics studies (e.g., Fischer et al. 2010, Fischer 2015). **Figure 12** shows a compilation of recent seismological estimates of the depth of the G-discontinuity (or seismic LAB) or the lithosphere thickness beneath the ocean. The data points are scattered, and if we take it that all observations are related to the same G-discontinuity (a velocity reduction from Lid to LVZ), no simple view emerges. As Rychert et al. (2012) noted, there appears to be some inconsistency among the various observations. Although these seeming inconsistencies might be caused by the stochastic nature of the LAS, as warned by Kennett & Yoshizawa (2016), here we attempt to synthesize the observations. Generally speaking, longer-period seismic data reflect larger-scale structures, such as the Lid/LVZ transition, and shorter-period data are sensitive to local properties, such as elongated flat scatterers (e.g., Shito et al. 2013, Kennett et al. 2014). If we assume that the longer-period SS-precursor observations (Rychert & Shearer 2011) give overall estimates of Lid/LVZ transition properties, compared to

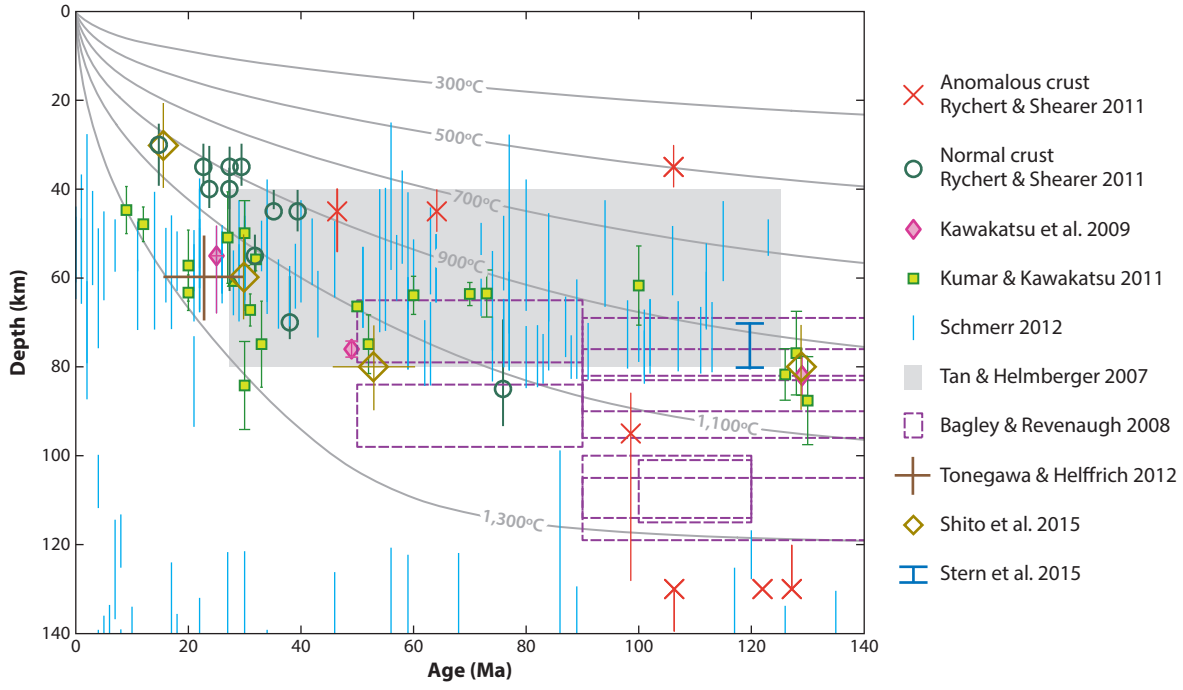

Figure 12

Discontinuity depth and plate thickness across the Pacific Ocean compared to seafloor age and plate model isotherms. Original data are from Rychert et al. (2012), and a few data points are deleted (Gaherty et al. 1999) or added (Shito et al. 2015, Stern et al. 2015, Tonegawa & Helffrich 2012).

the short-period ones (and if we exclude data points for anomalous crust), then the age dependence of the G-discontinuity or plate thickness seems to emerge (i.e., most points stay between 900°C and 1,200°C isotherms; see **Figure 12**). So both the overall seismic characteristics of the Lid/LVZ transition and the G-discontinuity may be understood as thermally controlled phenomena (see points 1 and 3 above).

The presence of laminar scatterers in the lithosphere and the observation that such a lithosphere grows with age may be most easily explained by underplating of laminar melts or melt pockets at the base of the lithosphere (as advocated by Kennett et al. 2014, Kennett & Furumura 2015, and Shito et al. 2015), which might also be observed via short-period SS precursors (Schmerr 2012). Such melts could result either from upwelling near ridges of small chemical heterogeneities that have low melting temperature (Hirschmann 2010) or from a variety of asthenospheric mantle upwellings, such as plumes (e.g., Phipps-Morgan et al. 1995), a general upward flow (Karato 2012), or small-scale convection (e.g., Korenaga & Jordan 2004). Such melt pockets are stretched with the shear due to corner flow near ridges (Blackman & Kendall 2002, Hirschmann 2010), or else simple shear due to plate motion produces shear-induced melt-rich bands (a millefeuille structure) in the asthenosphere (Holtzman et al. 2003, Takei & Holtzman 2009, Kawakatsu et al. 2009) that become part of the lithosphere as the LAS cools and that contribute to radial anisotropy in the LAS (Kawakatsu et al. 2009, Kennett & Furumura 2015) (see points 2 and 4). On subduction, such melts may not be able to follow the flow because of buoyancy, and may instead accumulate near the subduction corner (Naif et al. 2013) and cause petit-spot volcanism (Hirano et al. 2006) (**Figure 13**).

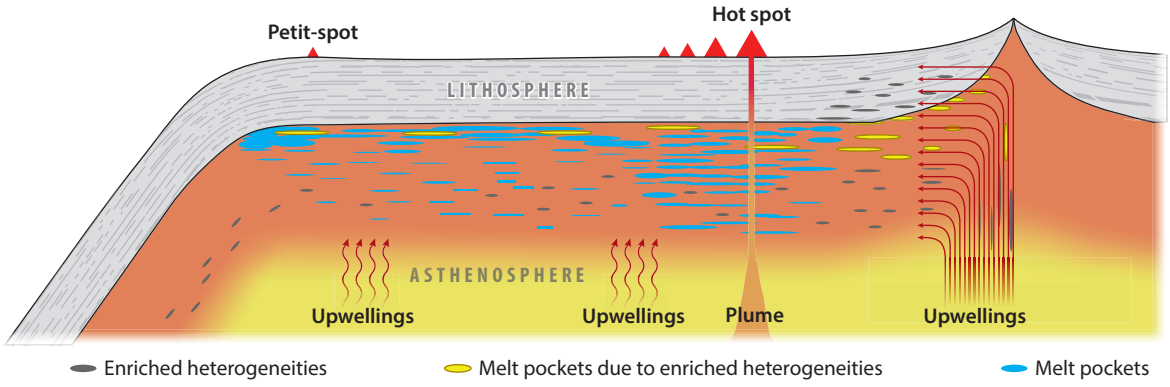

Figure 13

Diagram showing the synthesis made in Section 5: near ridges, enriched heterogeneities (*dark gray lenses*) develop melt pockets in the shallow parts of the low-velocity zone (LVZ) (*yellow lenses*) that will be stretched horizontally due to strong corner flow (Hirschmann 2010); other mantle upwellings will also introduce heat or volatiles in the LVZ to induce melting (*light blue lenses*) that will be also stretched horizontally to make connected networks (millefeuille asthenosphere; Kawakatsu et al. 2009). When these stretched melts solidify due to the plate cooling (underplating), laminar heterogeneities are accumulated at the base of lithosphere (e.g., Kennett & Furumura 2015).

From the electrical conductivity point of view, as discussed in connection with **Figure 9**, a thermally controlled LCL/HCL transition with stretching due to horizontal shear might be consistent with observations for the normal suboceanic mantle, if we consider near-plate boundary observations to be anomalous. Then available observations are in favor of partial melting as a cause of the HCL, although the effect of water is not ruled out. Electrical conductivity depends sensitively on connectivity of melt, and the LCL/HCL transition should be observed where the temperature is above solidus. In **Figure 9**, the LCL/HCL transition depths follow isotherms between 1,100°C and 1,200°C, possibly slightly higher (~100°C on average) than those for the Lid/LVZ transition. So both Lid/LVZ and LCL/HCL transitions may be understood as mainly controlled by thermal processes (see point 5). In addition, the relatively thick LCL (~80 km) reported by the MELT experiment (Evans et al. 2005) deserves explanation. It may be that horizontal melt connectivity is not yet effectively established, due to the low degree of shearing of the corner flow in the vicinity of the ridge.

5.2. Toward Comprehensive Views of the LAB and LAS

As mentioned in Section 1, the real LAB should be discussed in terms of the mechanical, rather than seismic or electrical, properties of the LAS. For this purpose, relations between physical and mechanical properties of the materials in the LAS materials should be established from a fundamental physical point of view, and this has not yet been achieved.

The synthesis made above may not be consistent with the view that the presence of water is the major controlling factor of the physical properties of the LAS (e.g., Karato 2012). Although there is no question of the importance of water in general, the degree to which water controls LAS properties deserves careful examination from both observational and theoretical/experimental points of view. As discussed in Section 1, there is still a lack of understanding of the basic physics involved. The synthesis presented here is based on reported observations; the need for more observational constraints is obvious, and we strongly feel that it can be resolved only by direct in situ seafloor observations.

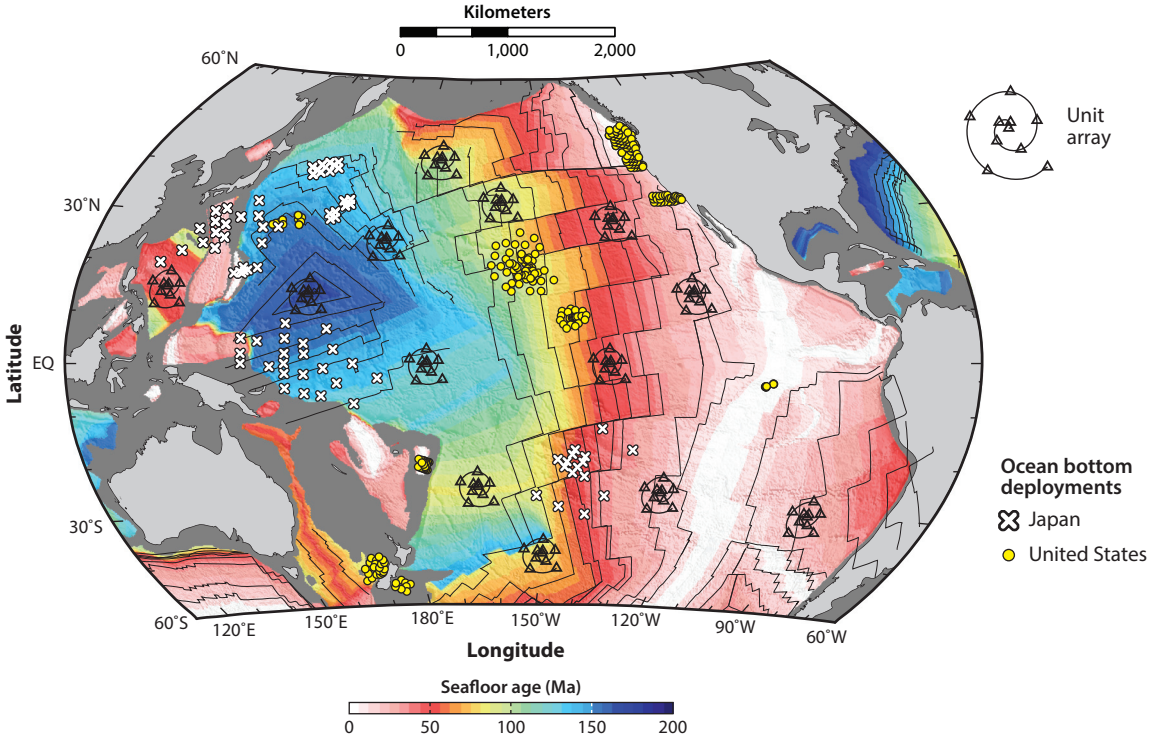

Figure 14

Conceptual image of proposed Pacific Array: A unit array here consists of ~10 BBOBSs/OBEMs, but actual array configuration should be carefully optimized. The location of unit arrays is also chosen ad hoc. White crosses and small yellow circles are existing ocean-bottom deployments conducted by Japanese and US scientists, respectively. Abbreviations: BBOBS, broadband ocean-bottom seismometer; OBEM, ocean-bottom electromagnetometer.

Recent advances in ocean-bottom geophysical observations, together with advances in analysis methodology, have now enabled us to resolve the regional 1-D structure of the entire LAS, from the surface to a depth of ~200 km, including seismic anisotropy (azimuthal), with deployments of ~10–15 BBOBSs and OBEMs, each for a year or so (Sections 3.2, 3.6). Thus, in situ characterization of the physical properties of the entire oceanic LAS without a priori assumptions for the most shallow structure, the assumptions often made for global studies, has become possible. We are now at an exciting stage in which large-scale array experiments in the ocean [e.g., the Pacific Array (**Figure 14**): **http://eri-ndc.eri.u-tokyo.ac.jp/PacificArray/**] have become approachable; such array observations, not only by giving regional constraints on 1-D structure (including seismic anisotropy) but also by sharing waveform data for global-scale waveform tomography (e.g., Fichtner et al. 2010, French et al. 2013, Zhu & Tromp 2013), should drastically increase our knowledge of how plate tectonics works beneath oceanic basins and help resolve the large-scale picture of the interior of the Earth.

DISCLOSURE STATEMENT

The authors are not aware of any affiliations, memberships, funding, or financial holdings that might be perceived as affecting the objectivity of this review.

ACKNOWLEDGMENTS

We thank Jun Korenaga for discussion; Takashi Furumura, Azusa Shito, Kate Rychert, and Akiko Takeo for figures; and Brian Kennett for a preprint. The members of the NOMan (Normal Oceanic Mantle) project helped us through their research. This research is partly supported by JSPS KAKENHI 22000003 and 15K13558.

LITERATURE CITED

Aki K. 1957. Space and time spectra of stationary stochastic waves with special reference to microtremors. *Bull. Earthq. Res. Inst.* 35:415–56

Aki K, Richards PG. 2002. *Quantitative Seismology*. Sausalito, CA: Univ. Sci. Books. 2nd ed.

Akuhara T, Mochizuki K, Kawakatsu H, Takeuchi N. 2016. Nonlinear waveform analysis for water-layer response and its application to high-frequency receiver function analysis using OBS array. *Geophys. J. Int.* 206:1914–20

Anderson DL, Sammis C. 1970. Partial melting in the upper mantle. *Phys. Earth Planet. Inter.* 3:41–50

Audet P. 2016. Receiver functions using OBS data: promises and limitations from numerical modelling and examples from the Cascadia Initiative. *Geophys. J. Int.* 205:1740–55

Baba K, Chave AD, Evans RL, Hirth G, Mackie RL. 2006. Mantle dynamics beneath the East Pacific Rise at 17°S: insights from the Mantle Electromagnetic and Tomography (MELT) experiment. *J. Geophys. Res.* 111:B02101

Baba K, Tada N, Zhang L, Liang P, Shimizu H, Utada H. 2013. Is the electrical conductivity of the western Pacific upper mantle normal? *Geochem Geophys. Geosyst.* 14:4969–79

Baba K, Utada H, Goto T, Kasaya T, Shimizu H, Tada N. 2010. Electrical conductivity imaging of the Philippine Sea upper mantle using seafloor magnetotelluric data. *Phys. Earth Planet. Inter.* 183:44–62

Bagley B, Courtierband AM, Revenaugh J. 2009. Melting in the deep upper mantle oceanward of the Honshu slab. *Phys. Earth Planet. Inter.* 175:137–44

Bagley B, Revenaugh J. 2008. Upper mantle seismic shear discontinuities of the Pacific. *J. Geophys. Res.* 113:B12301

Becker TW, Conrad CP, Schaeffer AJ, Lebedev S. 2014. Origin of azimuthal seismic anisotropy in oceanic plates and mantle. *Earth Planet. Sci. Lett.* 401:236–50

Blackman DK, Kendall JM. 2002. Seismic anisotropy in the upper mantle 2. Predictions for current plate boundary flow models. *Geochem. Geophys. Geosyst.* 3:8602

Booth CM, Forsyth DW, Weeraratne DS. 2014. Upper mantle Q structure beneath old seafloor in the western Pacific. *J. Geophys. Res. Solid Earth* 119:3448–61

Bozdağ E, Trampert J. 2008. On crustal corrections in surface wave tomography. *Geophys. J. Int.* 172:1066–1082

Burgos G, Montagner JP, Beucler E, Capdeville Y, Mocquet A, Drilleau M. 2014. Oceanic lithosphere/asthenosphere boundary from surface wave dispersion data. *J. Geophys. Res. Solid Earth* 119:1079–93

Cox C, Constable SC, Chave A, Webb SC. 1986. Controlled-source electromagnetic sounding of the oceanic lithosphere. *Nature* 320:52–54

Crosby AG, McKenzie D, Sclater JG. 2006. The relationship between depth, age and gravity in the oceans. *Geophys. J. Int.* 166:553–73

Dai L, Karato S. 2014. High and highly anisotropic electrical conductivity of the asthenosphere due to hydrogen diffusion in olivine. *Earth Planet. Sci. Lett.* 408:79–86

Dalton CA, Ekström G, Dziewonski AM. 2008. The global attenuation structure of the upper mantle. *J. Geophys. Res.* 113:B09303

Dalton CA, Ekström G, Dziewonski AM. 2009. Global seismological shear velocity and attenuation: a comparison with experimental observations. *Earth Planet. Sci. Lett.* 284:65–75

Debayle E, Ricard Y. 2013. Seismic observations of large-scale deformation at the bottom of fast-moving plates. *Earth Planet. Sci. Lett.* 376:165–77

Deuss A, Woodhouse JH. 2002. A systematic search for mantle discontinuities using SS-precursors. *Geophys. Res. Lett.* 29:90-1–90-4

Dorman J, Ewing M, Oliver J. 1960. Study of shear-velocity distribution in the upper mantle by mantle Rayleigh waves. *Bull. Seismol. Soc. Am.* 50:87–115

Dunn RA, Forsyth DW. 2003. Imaging the transition between the region of mantle melt generation and the crustal magma chamber beneath the southern East Pacific Rise with short-period Love waves. *J. Geophys. Res.* 108(B7):2352

Dziewonski AM, Anderson DL. 1981. Preliminary reference Earth model. *Phys. Earth Planet. Inter.* 25:297–356

Ekström G, Dziewonski AM. 1998. The unique anisotropy of the Pacific upper mantle. *Nature* 394:168–72

Evans RL, Hirth G, Baba K, Forsyth D, Chave A, Mackie R. 2005. Geophysical evidence from the MELT area for compositional controls on oceanic plates. *Nature* 437:249–52

Evans RL, Tarits P, Chave AD, White A, Heinson G, et al. 1999. Asymmetric electrical structure in the mantle beneath the East Pacific Rise at 17°S. *Science* 286:752–55

Fei H, Wiedenbeck M, Yamasaki D, Katsura T. 2013. Small effect of water on upper-mantle rheology based on silicon self-diffusion coefficients. *Nature* 498:213–15

Ferreira AMG, Woodhouse JH, Visser K, Trampert J. 2010. On the robustness of global radially anisotropic surface wave tomography. *J. Geophys. Res.* 115:B04313

Fichtner A, Kennett B, Igel H, Bunge HP. 2010. Full waveform tomography for radially anisotropic structure: new insights into present and past states of the Australasian upper mantle. *Earth Planet. Sci. Lett.* 290:270–80

Fischer KM. 2015. Seismological constraints on the lithosphere–asthenosphere boundary. In *Treatise on Geophysics*, Vol. 1: *Deep Earth Seismology*, ed. G Schubert, pp. 587–612. Amsterdam: Elsevier. 2nd ed.

Fischer KM, Ford HA, Abt DL, Rychert CA. 2010. The lithosphere–asthenosphere boundary. *Annu. Rev. Earth Planet. Sci.* 38:551–75

Forsyth DW. 1975. The early structural evolution and anisotropy of the oceanic upper mantle. *Geophys. J. R. Astron. Soc.* 43:103–62

Forsyth DW, Li A. 2005. Array analysis of two-dimensional variations in surface wave phase velocity and azimuthal anisotropy in the presence of multipathing interference. In *Seismic Earth: Array Analysis of Broadband Seismograms*, ed. A Levander, G Nolet, pp. 81–97. Washington, DC: Am. Geophys. Union

Foster A, Nettles M, Ekström G. 2014. Overtone interference in array-based Love-wave phase measurements. *Bull. Seismol. Soc. Am.* 104:2266–77

French S, Lekic V, Romanowicz B. 2013. Waveform tomography reveals channeled flow at the base of the oceanic asthenosphere. *Science* 342:227–30

Furumura T, Kennett BLN. 2005. Subduction zone guided waves and the heterogeneity structure of the subducted plate: intensity anomalies in northern Japan. *J. Geophys. Res.* 110:B10302

Gaherty JB, Kato M, Jordan TH. 1999. Seismological structure of the upper mantle: a regional comparison of seismic layering. *Phys. Earth Planet. Inter.* 110:21–41

Gaherty JB, Lizarralde D, Collins JA, Hirth G, Kim S. 2004. Mantle deformation during slow seafloor spreading constrained by observations of seismic anisotropy in the western Atlantic. *Earth Planet. Sci. Lett.* 228:255–65

Gaillard F, Mohammed M, Iacono-Marziano G, Pichavant M, Scaillet B. 2008. Carbonatite melts and electrical conductivity in the asthenosphere. *Science* 322:1363–65

Gardes E, Gaillard F, Tarits P. 2014. Toward a unified hydrous olivine electrical conductivity law. *Geochem. Geophys. Geosyst.* 15:4984–5000

Gu YJ, Dziewonski AM, Ekström G. 2001. Lehmann discontinuity beneath continents. *Geophys. Res. Lett.* 28:4655–58

Gutenberg B. 1959. *Physics of the Earth's Interior*. New York: Elsevier

Harmon N, Forsyth D, Webb S. 2007. Using ambient seismic noise to determine short-period phase velocities and shallow shear velocities in young oceanic lithosphere. *Bull. Seismol. Soc. Am.* 97:2009–23

Hirano N, Takahashi E, Yamamoto J, Abe N, Ingle SP, et al. 2006. Volcanism in response to plate flexure. *Science* 313:1426–28

Hirschmann MM. 2010. Partial melt in the oceanic low velocity zone. *Phys. Earth Planet. Inter.* 179:60–71

Hirschmann MM, Dasgupta R. 2009. The H/C ratios of Earth's near-surface and deep reservoirs, and consequences for deep Earth volatile cycles. *Chem. Geol.* 262:4–16

Holtzman BK, Kohlstedt DL, Zimmerman ME, Heidelbach F, Hiraga T, Hustoft J. 2003. Melt segregation and strain partitioning: implications for seismic anisotropy and mantle flow. *Science* 301:1227–30

Jackson I, Faul UH, Skelton R. 2014. Elastically accommodated grain-boundary sliding: new insights from experiment and modeling. *Phys. Earth Planet. Inter.* 228:203–10

Jung H, Katayama I, Jian Z, Hiraga T, Karato S. 2006. Effect of water and stress on the lattice-preferred orientation of olivine. *Tectonophysics* 421:1–22

Kaneda K, Kodaira S, Nishizawa A, Morishita T, Takahashi N. 2010. Structural evolution of preexisting oceanic crust through intraplate igneous activities in the Marcus–Wake seamount chain. *Geochem. Geophys. Geosyst.* 11:Q10014

Karato S. 2012. On the origin of the asthenosphere. *Earth Planet. Sci. Lett.* 321–322:95–103

Kawakatsu H. 2016. A new fifth parameter for transverse isotropy. *Geophys. J. Int.* 204:682–85

Kawakatsu H, Kumar P, Takei Y, Shinohara M, Kanazawa T, et al. 2009. Seismic evidence for sharp lithosphere–asthenosphere boundaries of oceanic plates. *Science* 324:499–502

Kelbert A, Kuvshinov A, Veláský J, Toyama T, Ribaudo J, et al. 2014. Global 3-D electromagnetic forward modelling: a benchmark study. *Geophys. J. Int.* 197:785–814

Kennett BLN, Furumura T. 2013. High-frequency Po/So guided waves in the oceanic lithosphere: I—long-distance propagation. *Geophys. J. Int.* 195:1862–77

Kennett BLN, Furumura T. 2015. Toward the reconciliation of seismological and petrological perspectives on oceanic lithosphere heterogeneity. *Geochem. Geophys. Geosyst.* 16:3129–41

Kennett BLN, Furumura T, Zhao Y. 2014. High-frequency Po/So guided waves in the oceanic lithosphere: II—heterogeneity and attenuation. *Geophys. J. Int.* 199:614–30

Kennett BLN, Yoshizawa K. 2017. Lithospheric discontinuities beneath Australia: interaction of large-scale and fine-scale structure. In *Lithospheric Discontinuities*, ed. H Yuan, B Romanowicz, AG Jones. Washington, DC: Am. Geophys. Union. In press

Key K, Constable S, Liu L, Pommier A. 2013. Electrical image of passive mantle upwelling beneath the northern East Pacific Rise. *Nature* 495:499–502

Key K, Constable S, Matsuno T, Evans R, Myer D. 2012. Electromagnetic detection of plate hydration due to bending faults at the Middle America Trench. *Earth Planet. Sci. Lett.* 351–352:45–53

Korenaga J, Jordan TH. 2004. Physics of multiscale convection in Earth's mantle: evolution of sublithospheric convection. *J. Geophys. Res.* 109:B01405

Kumar P, Kawakatsu H. 2011. Imaging the seismic lithosphere–asthenosphere boundary of the oceanic plate. *Geochem. Geophys. Geosyst.* 12:Q01006

Kumar P, Kawakatsu H, Shinohara M, Kanazawa T, Araki E, Suyehiro K. 2011. P and S receiver function analysis of seafloor borehole broadband seismic data. *J. Geophys. Res.* 116:B12308

Kustowski B, Ekström G, Dziewonski AM. 2008. Anisotropic shear-wave velocity structure of the Earth's mantle: a global model. *Earth Planet. Sci. Lett.* 113:B06306

Leeds AR, Knopo L, Kausel EG. 1974. Variations of upper mantle structure under the Pacific Ocean. *Science* 186:141–43

Lévêque JJ, Cara M. 1985. Inversion of multimode surface wave data: evidence for sub-lithospheric anisotropy. *Geophys. J. R. Astron. Soc.* 83:753–73

Lin FC, Ritzwoller MH, Yang Y, Moschetti MP, Fouch MJ. 2010. Complex and variable crustal and uppermost mantle seismic anisotropy in the western United States. *Nat. Geosci.* 4:55–61

Lizarralde D, Gaherty JB, Collins JA, Hirth G, Kim SD. 2004. Spreading-rate dependence of melt extraction at mid-ocean ridges from mantle seismic refraction data. *Nature* 432:744–47

Long M, Silver PG. 2008. The subduction zone flow field from seismic anisotropy: a global view. *Science* 319:315–18

MacGregor L, Sinha M, Constable S. 2001. Electrical resistivity structure of the Valu Fa Ridge, Lau Basin, from marine controlled-source electromagnetic sounding. *Geophys. J. Int.* 146:217–36

Maggi A, Debayle E, Priestley K, Barruol G. 2006a. Azimuthal anisotropy of the Pacific region. *Earth Planet. Sci. Lett.* 250:53–71

Maggi A, Debayle E, Priestley K, Barruol G. 2006b. Multimode surface waveform tomography of the Pacific Ocean: a closer look at the lithospheric cooling signature. *Geophys. J. Int.* 166:1384–97

Mainprice D. 2015. Seismic anisotropy of the deep Earth from a mineral and rock physics perspective. In *Treatise on Geophysics*, Vol. 2: *Mineral Physics*, ed. G Schubert, pp. 487–538. Amsterdam: Elsevier. 2nd ed.
Matsuno T, Seama N, Evans RL, Chave AD, Baba K, et al. 2010. Upper mantle electrical resistivity structure beneath the central Mariana subduction system. *Geochem. Geophys. Geosyst.* 11:Q09003
Matsuno T, Suetsugu D, Baba K, Tada N, Shimizu H, et al. 2017. Mantle transition zone beneath a normal seafloor in the northwestern Pacific: electrical conductivity, seismic thickness, and water content. *Earth Planet. Sci. Lett.* 462:189–98
McKenzie D, Jackson J, Priestley K. 2005. Thermal structure of oceanic and continental lithosphere. *Earth Planet. Sci. Lett.* 233:337–49
Mei S, Kohlstedt DL. 2000a. Influence of water on plastic deformation of olivine aggregates. 1. Diffusion creep regime. *J. Geophys. Res.* 105:21457–69
Mei S, Kohlstedt DL. 2000b. Influence of water on plastic deformation of olivine aggregates. 2. Dislocation creep regime. *J. Geophys. Res.* 105:21471–81
Montagner JP. 1985. Seismic anisotropy of the Pacific Ocean inferred from long-period surface waves dispersion. *Phys. Earth Planet. Inter.* 38:28–50
Naif S, Key K, Constable S, Evans RL. 2013. Melt-rich channel observed at the lithosphere-asthenosphere boundary. *Nature* 495:356–59
Nettles M, Dziewonski AM. 2008. Radially anisotropic shear velocity structure of the upper mantle globally and beneath North America. *J. Geophys. Res.* 113:B02303
Nettles M, Dziewoński AM. 2011. Effect of higher-mode interference on measurements and models of fundamental-mode surface-wave dispersion. *Bull. Seismol. Soc. Am.* 101:2270–80
Nishida K, Kawakatsu H, Obara K. 2008. Three-dimensional crustal S-wave velocity structure in Japan using microseismic data recorded by Hi-net tiltmeters. *J. Geophys. Res.* 113:B10302
Nishimura CE, Forsyth DW. 1989. The anisotropic structure of the upper mantle in the Pacific. *Geophys. J. Int.* 96:203–29
Parsons B, McKenzie D. 1978. Mantle convection and the thermal structure of the plates. *J. Geophys. Res.* 83:4485–96
Parsons B, Sclater J. 1977. An analysis of the variation of ocean floor bathymetry and heat flow with age. *J. Geophys. Res.* 82:803–27
Phipps-Morgan J, Morgan WJ, Zhang YS, Smith WHF. 1995. Observational hints for a plume-fed, suboceanic asthenosphere and its role in mantle convection. *J. Geophys. Res.* 100:12753–67
Pommier A, Leinenweber K, Kohlstedt D, Chao Q, Garnero E, et al. 2015. Experimental constraints on the electrical anisotropy of the lithosphere-asthenosphere system. *Nature* 522:202–6
Priestley K, McKenzie D. 2006. The thermal structure of the lithosphere from shear wave velocities. *Earth Planet. Sci. Lett.* 244:285–301
Priestley K, McKenzie D. 2013. The relationship between shear wave velocity, temperature, attenuation and viscosity in the shallow part of the mantle. *Earth Planet. Sci. Lett.* 381:78–91
Raitt RW, Shor GG, Francis TJG, Morris GB. 1969. Anisotropy of the Pacific upper mantle. *J. Geophys. Res.* 74:3095–109
Revenaugh J, Jordan TH. 1991. Mantle layering from ScS reverberations: 3. The upper mantle. *J. Geophys. Res.* 96:781–810
Richards MA, Yang WS, Baumgardner JR, Bunge HP. 2001. Role of a low-viscosity zone in stabilizing plate tectonics: implications for comparative terrestrial planetology. *Geochem. Geophys. Geosyst.* 2:1026
Ritzwoller MH, Shapiro NM, Zhong SJ. 2004. Cooling history of the Pacific lithosphere. *J. Geophys. Res.* 226:69–84
Roth EG, Wiens DA, Dorman LM, Hildebrand J, Webb SC. 1999. Seismic attenuation tomography of the Tonga-Fiji region using phase pair methods. *J. Geophys. Res.* 104(B3):4795–809
Rychert CA, Schmerr N, Harmon N. 2012. The Pacific lithosphere–asthenosphere boundary: seismic imaging and anisotropic constraints from SS waveforms. *Geochem. Geophys. Geosyst.* 13:Q0AK10
Rychert CA, Shearer PM. 2011. Imaging the lithosphere–asthenosphere boundary beneath the Pacific using SS waveform modeling. *J. Geophys. Res.* 116:B07307
Schaeffer AJ, Lebedev S. 2013. Global shear speed structure of the upper mantle and transition zone. *Geophys. J. Int.* 194:417–49

Schlue JW, Knopoff L. 1977. Shear-wave polarization anisotropy in the Pacific Basin. *Geophys. J. R. Astron. Soc.* 49:145–65

Schmerr N. 2012. The Gutenberg discontinuity: melt at the lithosphere-asthenosphere boundary. *Science* 335:1480–83

Shankland TJ, Waff HS. 1977. Partial melting and electrical conductivity anomalies in the upper mantle. *J. Geophys. Res.* 82:5409–17

Shapiro NM, Campillo M, Stehly L, Ritzwoller MH. 2005. High-resolution surface-wave tomography from ambient seismic noise. *Science* 307:1615–18

Shimamura H, Asada T, Suyehiro K, Yamada T, Inatani H. 1983. Longshot experiments to study velocity anisotropy in the oceanic lithosphere of the northwestern Pacific. *Phys. Earth Planet. Inter.* 31:348–62

Shinohara M, Fukano T, Kanazawa T, Araki E, Suyehiro K, et al. 2008. Upper mantle and crustal seismic structure beneath the northwestern Pacific basin using a seafloor borehole broadband seismometer and ocean bottom seismometers. *Phys. Earth Planet. Inter.* 170:95–106

Shito A, Suetsugu D, Furumura T. 2015. Evolution of the oceanic lithosphere inferred from Po/So waves traveling in the Philippine Sea Plate. *J. Geophys. Res. Solid Earth* 120:5238–48

Shito A, Suetsugu D, Furumura T, Sugioka H, Ito A. 2013. Small-scale heterogeneities in the oceanic lithosphere inferred from guided waves. *Geophys. Res. Lett.* 40:1708–12

Smith DB, Ritzwoller MH, Shapiro NM. 2004. Stratification of anisotropy in the Pacific upper mantle. *J. Geophys. Res.* 109:B11309

Song TRA, Kawakatsu H. 2012. Subduction of oceanic asthenosphere: evidence from sub-slab seismic anisotropy. *Geophys. Res. Lett.* 39:L17301

Song TRA, Kawakatsu H. 2013. Subduction of oceanic asthenosphere: a critical appraisal in central Alaska. *Earth Planet. Sci. Lett.* 367:82–94

Song TRA, Kim YH. 2011. Anisotropic uppermost mantle in young subducted slab underplating Central Mexico. *Nat. Geosci.* 5:55–59

Stern TA, Henrys SA, Okaya D, Louie JN, Savage MK, et al. 2015. A seismic reflection image for the base of a tectonic plate. *Nature* 518:85–90

Stixrude L, Lithgow-Bertelloni C. 2005. Mineralogy and elasticity of the oceanic upper mantle: origin of the low-velocity zone. *J. Geophys. Res.* 110:B03204

Suetsugu D, Shiobara H. 2014. Broadband ocean-bottom seismology. *Annu. Rev. Earth Planet. Sci.* 42:27–43

Tada N, Baba K, Utada H. 2014. Three-dimensional inversion of seafloor magnetotelluric data collected in the Philippine Sea and the western margin of the northwest Pacific Ocean. *Geochem. Geophys. Geosyst.* 15:2895–917

Takei Y. 2002. Effect of pore geometry on V_p/V_s: from equilibrium geometry to crack. *J. Geophys. Res.* 107(B2):ECV6-1–12

Takei Y, Holtzman BK. 2009. Viscous constitutive relations of solid–liquid composites in terms of grain boundary contiguity: 1. Grain boundary diffusion control model. *J. Geophys. Res.* 114:B06205

Takei Y, Karasawa F, Yamauchi H. 2014. Temperature, grain size, and chemical controls on polycrystal anelasticity over a broad frequency range extending into the seismic range. *J. Geophys. Res. Solid Earth* 119:5414–43

Takeo A, Kawakatsu H, Isse T, Nishida K, Sugioka H, et al. 2016. Seismic azimuthal anisotropy in the oceanic lithosphere and asthenosphere from broadband surface wave analysis of OBS array records at 60 Ma seafloor. *J. Geophys. Res. Solid Earth* 121:1927–47

Takeo A, Nishida K, Isse T, Kawakatsu H, Shiobara H, et al. 2013. Radially anisotropic structure beneath the Shikoku Basin from broadband surface wave analysis of ocean bottom seismometer records. *J. Geophys. Res. Solid Earth* 118:1–15

Takeuchi H, Press F, Kobayashi N. 1959. Rayleigh-wave evidence for the low-velocity zone in the mantle. *Bull. Seismol. Soc. Am.* 49:355–64

Tan Y, Helmberger DV. 2007. Trans-Pacific upper mantle shear velocity structure. *J. Geophys. Res.* 112:B08301

Tanimoto T, Anderson DL. 1984. Mapping convection in the mantle. *Geophys. Res. Lett.* 11:287–90

Tommasi A, Ishikawa A. 2014. Microstructures, composition, and seismic properties of the Ontong Java Plateau mantle root. *Geochem. Geophys. Geosyst.* 15:4547–69

Tonegawa T, Helffrich G. 2012. Basal reflector under the Philippine Sea Plate. *Geophys. J. Int.* 189:659–68
Toomey DR, Jousselin D, Dunn RA, Wilcock WSD, Detrick RS. 2007. Skew of mantle upwelling beneath the East Pacific Rise governs segmentation. *Nature* 446:409–14
Toramaru A, Fujii N. 1986. Connectivity of melt phase in a partially molten peridotite. *J. Geophys. Res.* 91:9239–52
Utada H. 2015. Electromagnetic exploration of the oceanic mantle. *Proc. Jpn. Acad. B* 91:390–405
Utada H, Baba K. 2014. Estimating the electrical conductivity of the melt phase of a partially molten asthenosphere from seafloor magnetotelluric sounding data. *Phys. Earth Planet. Inter.* 227:41–47
Walker DA. 1977. High-frequency Pn phases observed in the Pacific at great distances. *Science* 197:257–59
Weeraratne DS, Forsyth DW, Yang Y, Webb SC. 2007. Rayleigh wave tomography beneath intraplate volcanic ridges in the South Pacific. *J. Geophys. Res.* 112:B06303
White R, McKenzie D, O'Nions R. 1992. Oceanic crustal thickness from seismic measurements and rare earth element inversions. *J. Geophys. Res.* 97:19683–715
Yang Y, Forsyth DW, Weeraratne DS. 2007. Seismic attenuation near the East Pacific Rise and the origin of the low-velocity zone. *Earth Planet. Sci. Lett.* 258:260–68
Yoshii T, Kono Y, Ito K. 1976. Thickening of the oceanic lithosphere. In *The Geophysics of the Pacific Ocean Basin and Its Margin*, ed. GH Sutton, MH Manghnani, R Moberly, EU McAfee, pp. 423–30. Washington, DC: Am. Geophys. Union
Yoshino T, Katsura T. 2013. Electrical conductivity of mantle minerals: effects of water in conductivity anomalies. *Annu. Rev. Earth Planet. Sci.* 41:605–28
Yoshizawa K. 2014. Radially anisotropic 3-D shear wave structure of the Australian lithosphere and asthenosphere from multi-mode surface waves. *Phys. Earth Planet. Inter.* 235:33–48
Zhu H, Tromp J. 2013. Mapping tectonic deformation in the crust and upper mantle beneath Europe and the North Atlantic Ocean. *Science* 341:871–75

Annual Review
of Earth and
Planetary Sciences
Volume 45, 2017

Contents

Errata

An online log of corrections to *Annual Review of Earth and Planetary Sciences* articles may be found at http://www.annualreviews.org/errata/earth